UNIVERSITY OF HELSINKI REPORT SERIES IN PHYSICS

HU-P-D128

LUNG STRUCTURE AND FUNCTION STUDIED BY SYNCHROTRON RADIATION

Liisa Porra

Division of X-ray Physics
Department of Physical Sciences
Faculty of Science
and
Department of Clinical Physiology
and Nuclear Medicine
Faculty of Medicine
University of Helsinki
Helsinki, Finland

ACADEMIC DISSERTATION

To be presented, with the permission of the Faculty of Science of the University of Helsinki, for public criticism in Auditorium B123 of Exactum on 21th April 2006, at 14 o'clock.

Helsinki 2006

Supervised by:

Professor Pekka Suortti
Division of X-ray Physics
Department of Physical Sciences
Faculty of Science
University of Helsinki
Finland

Professor Anssi Sovijärvi
Department of Clinical Physiology
and Nuclear Medicine
Faculty of Medicine
University of Helsinki
Finland

Reviewed by:

Professor Manuel Paiva
Laboratoire de Physique Biomédicale
Université Libre de Bruxelles
Belgium

Professor Raimo Sepponen
Department of Electrical and
Communications Engineering
Helsinki University of Technology
Finland

Opponent:

Professor Pekka Meriläinen
Department of Engineering Physics and Mathematics
Helsinki University of Technology
Finland

Report Series in Physics HU-P-D128
ISSN 0356-0961
ISBN 952-10-2111-X
ISBN 952-10-2112-8 (pdf-version)
http://www.ethesis.helsinki.fi
Helsinki 2006
Yliopistopaino

L. Porra: Lung structure and function studied by synchrotron radiation, University of Helsinki, 2006, 79 pages + appendices. University of Helsinki, Report Series in Physics, HU-P-D128.

ABSTRACT

A novel method for functional lung imaging was introduced by adapting the K-edge subtraction method (KES) to *in vivo* studies of small animals. In this method two synchrotron radiation energies, which bracket the K-edge of the contrast agent, are used for simultaneous recording of absorption-contrast images. Stable xenon gas is used as the contrast agent, and imaging is performed in projection or computed tomography (CT) mode. Subtraction of the two images yields the distribution of xenon, while removing practically all features due to other structures, and the xenon density can be calculated quantitatively. Because the images are recorded simultaneously, there are no movement artifacts in the subtraction image. Time resolution for a series of CT images is one image/s, which allows functional studies. Voxel size is 0.1mm^3, which is an order better than in traditional lung imaging methods.

KES imaging technique was used in studies of ventilation distribution and the effects of histamine-induced airway narrowing in healthy, mechanically ventilated, and anaesthetized rabbits. First, the effect of tidal volume on ventilation was studied, and the results show that an increase in tidal volume without an increase in minute ventilation results a proportional increase in regional ventilation. Second, spiral CT was used to quantify the airspace volumes in lungs in normal conditions and after histamine aerosol inhalation, and the results showed large patchy filling defects in peripheral lungs following histamine provocation. Third, the kinetics of proximal and distal airway response to histamine aerosol were examined, and the findings show that the distal airways react immediately to histamine and start to recover, while the reaction and the recovery in proximal airways is slower. Fourth, the fractal dimensions of lungs was studied, and it was found that the fractal dimension is higher at the apical part of the lungs compared to the basal part, indicating structural differences between apical and basal lung level.

These results provide new insights to lung function and the effects of drug challenge studies. Nowadays the technique is available at synchrotron radiation facilities, but the compact synchrotron radiation sources are being developed, and in relatively near future the method may be used at hospitals.

Classification (INSPEC): A8710, A8745F, A8745H, A8760J

Keywords: synchrotron radiation, imaging, xenon, airway structure, distribution of ventilation, broncho-constriction, asthma

PREFACE

This thesis is based on research carried out at the Division of X-ray Physics of the Department of Physical Sciences at the University of Helsinki, and at the medical beamline ID17 of the European Synchrotron Radiation Facility in Grenoble, France. I wish to thank Prof. Juhani Keinonen for providing me the opportunity to work at the Department of Physical Sciences, and Prof. Keijo Hämäläinen for all the support at the Division of X-ray Physics.

My special thanks belong to my supervisors Prof. Pekka Suortti and Prof. Anssi Sovijärvi for introducing me to the interesting field of synchrotron radiation, medical physics, and physiology. I am really grateful that I have been able to work under your supervision, and I would like to thank you for the guidance and encouragement you have given me throughout this work. I would also like to thank Prof. Manuel Paiva from Université Libre de Bruxelles, and Prof. Raimo Sepponen from Helsinki University of Technology for reviewing this thesis and giving me valuable comments.

I would like to thank Dr. Sam Bayat from France for all the help during these years. This work could not have been feasible without him. I wish also thank the personnel at the X-ray laboratory for creating an inspiring working atmosphere. Especially I would like to thank Manuel Fernández, Jani Keyriläinen, and Heikki Suhonen for interesting discussions, and their important contribution in the research. The help from the personnel of the European Synchrotron Radiation Facility has also been important; especially I would like to thank Sylvie Monfraix and Christian Nemoz.

Finally, I want to deeply thank my family and friends for their continuous love, support, and care during these years.

The work was funded by the Academy of Finland, by the University of Helsinki, by the Helsinki University Central Hospital, by the Paulo Foundation, by the Ida Montin Foundation, by the Foundation of Vilho, Yrjö and Kalle Väisälä, and by the Instrumentarium Foundation for Science.

Helsinki, March 16, 2006

Liisa Porra

CONTENTS

LIST OF ORIGINAL ARTICLES

This thesis consists of the following scientific articles, which are referred to by Roman numerals **I** – **IV** throughout the text.

I S. Bayat, G. Le Duc, L. Porra, G. Berruyer, C. Nemoz, S. Monfraix, S. Fiedler, W. Thomlinson, , P. Suortti, C.G. Standertskjöld-Nordenstam, A.R.A. Sovijärvi: *Quantitative functional lung imaging by synchrotron radiation using stable xenon gas as contrast agent*, Phys Med Biol **46**: 3287–3299 (2001).

II L. Porra, S. Monfraix, G. Berruyer, C. Nemoz, G. Le Duc, W. Thomlinson, P. Suortti, A.R.A. Sovijärvi and S. Bayat: *Effect of tidal volume on distribution of ventilation assessed by synchrotron radiation CT in rabbit*, J Appl Physiol **96**: 1899–1908 (2004).

III S. Monfraix, S. Bayat, L. Porra, G. Berruyer, C. Nemoz, W. Thomlinson, P. Suortti, and A.R.A. Sovijärvi: *Quantitative measurement of regional lung gas volume by synchrotron radiation computed tomography*, Phys Med Biol **50**: 1–11 (2005).

IV S. Bayat, L. Porra, H. Suhonen, C. Nemoz, P. Suortti and A.R.A. Sovijärvi: *Differences in the time course of proximal and distal airway response to inhaled histamine studied by synchrotron radiation CT*, J Appl Physiol, **in press**, February 9, 2006, doi:10.1152/japplphysiol.00594-2005.

SYMBOLS AND ABBREVIATIONS

$\left(\frac{\mu}{\rho}\right)$	Mass absorption coefficient
$\left(\frac{\mu_{en}}{\rho}\right)$	Mass energy absorption coefficient
η	Elastance
Φ	Photon flux
μ	Absorption coefficient
ρ	Density
τ	Time constant
A	Area
D	Fractal dimension
$D(t)$	Density (in time)
D_0	Initial density
D_{as}	Asymptotic density
E	Energy
E_K	K-edge energy
G	Conductance
I	Intensity
I_0	Incident intensity
l	Length
l_0	Initial length
L	Curve length ($L(l)$)
N	Number
N_0	Number of photons
p	Pressure
P_A	Arterial pressure
P_{TR}	Tracheal pressure
Q	Charge
r	Radius
R	Resistance
$s\dot{V}$	Specific ventilation (V/V_0)
t	Time
v	Velocity
$\overline{v}$	Mean velocity
V	Volume
V_0	Voxel volume
V_{as}	Asymptotic volume
$\dot{V}$	Ventilation (dV/dt)
$(\dot{V}_A/\dot{Q})$	Ventilation/perfusion ratio
x	Thickness

CT	Computed tomography
CV	Coefficient of variation (mean/SD)
FRC	Functional residual capacity
FMS	Fluorescent microspheres
FWHM	Full-width at half-maximum
HU	Hounsfield units
KES	K-edge subtraction imaging
MRI	Magnetic resonance imaging
PET	Positron emission tomography
ROI	Region of interest
RV	Residual volume
SNR	Signal to noise ratio
SSR	Summed squared residuals
SPECT	Single photon emission computed tomography
TLC	Total lung capacity
UV	Unit of ventilation
VT	Tidal volume

1. INTRODUCTION

The ability to quantify the regional distribution of air volume within the lung would provide a valuable tool for the study of regional lung function and give access to the measurement of regional lung mechanical properties. In mechanically ventilated subjects, factors such as regional lung mechanics, ventilation modes, and the presence of pathology, all affect the distribution of inspired air. Non-invasive methods to study the impact of such factors on the regional distribution of ventilation are currently needed [Frerichs et al., 2002].

The use of imaging technique allows an access to a local information, which is not possible with spirometry giving global lung volumes and ventilation indications. Ideally, the imaging method should have a spatial resolution allowing to image small airspaces, and the signal should come from the gas itself. At the same time, the temporal resolution should be sufficient for *in vivo* functional studies.

The spatial resolution of the modern thorax computed tomography (CT) scanners is of the order of 1 mm^3 and the regional air and tissue content can be estimated from a conversion of Hounsfield units. However, this measurement does not allow the distinction of well vs. poorly ventilated peripheral air spaces of the lungs. A direct signal from the gas itself is obtained by scintigraphic methods [Gefter, 2002], xenon-enhanced CT [Marcucci et al., 2001], and by the use of hyper-polarized ^{3}He in magnetic resonance imaging (MRI) [Middleton et al., 1995]. The limitations arise from the weak signal, low spatial and/or temporal resolution, and from interactions of the marker gas with the lung tissue. The spatial, temporal and contrast resolution are related to each other, because for a signal sufficiently above the noise level a minimum voxel size and acquisition time are required. The acquisition time is limited by motion artifacts, gas interactions with the tissue and by the radiation dose in the cases where x-rays or radioactive markers are used. Distribution of ventilation can be also studied with fluorescent microspheres aerosol method by measuring the fluorescent signal in cut lung pieces. The resolution is adequate for ventilation studies, but the animal is sacrificed before imaging, which changes the conditions, and the experiments can not be repeated with the same animal [Altemeier et al., 2000]. There is a need for quantitative methods to study the distribution of ventilation with high resolution.

Most studies of airway reactivity have been performed *in-vitro*, with a video microscopy using precision-cut lung slices [Martin et al., 1996]. Airway narrowing is caused by agonists like histamine and methacholine. *In vivo* imaging of airway narrowing has been performed with high-resolution CT [Brown and Mitzner, 1998]. The results give high-resolution images from airway narrowing, but the method does not show the changes in the distribution of ventilation at the same time. Changes in the distribution of ventilation during airway narrowing has been studied with PET [Vidal Melo et al., 2005]. The resolution is adequate to study the distribution of ventilation in 3D, but images does not show any information from the airways. There is a strong need of imaging methods, where the distribution of ventilation, and changes in airways can be studied simultaneously.

We propose a new approach for direct measurement of regional lung mechanics, using synchrotron radiation with K-edge subtraction imaging (KES). KES imaging method visualizes stable xenon gas used as an inhaled contrast agent, and it is possible to directly quantify its absolute density on any given point of a lung CT image [Bayat et al., 2001]. A significant advantage of this technique is the good spatial resolution (pixel size: 350 μm, voxel size 0.1 mm^3) allowing functional imaging studies in small animal experimental models. High-resolution images of ventilation distribution, and anatomic CT images, are imaged simultaneously, which gives possibility to study the anatomical and physiological changes together. This method has been applied to study the regional ventilation and lung volume, and airway diameters in normal conditions and after histamine-induced airway narrowing.

2. BACKGROUND

2.1 Respiratory system

The chart of the respiratory system of humans (figure 2.1) shows the lung structure. Breathing brings the oxygen (O_2) in the air into the lungs and into close contact with the blood, which absorbs it and carries it to all parts of the body. At the same time the blood delivers the carbon dioxide (CO_2), which is carried out of the lungs when air is breathed out. The trachea leads from the throat to the lungs. The trachea branches into the two main bronchi, one for each lung, which branches into each lobe of the lungs. The right lung is divided into three lobes. Each lobe is like a balloon filled with sponge-like tissue. The left lung is divided into two lobes [Nienstedt et al., 1992].

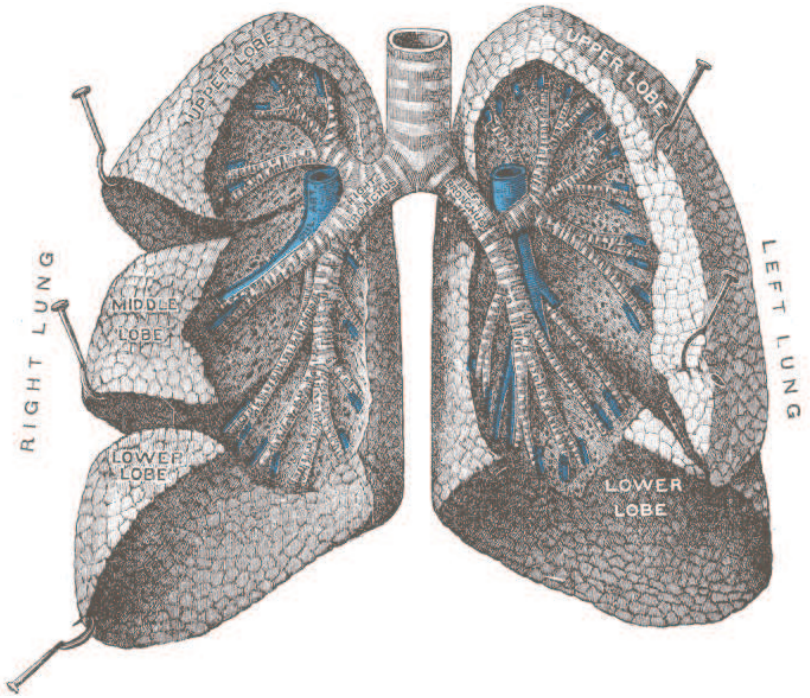

Fig. 2.1: Human respiratory system [Gray, 1918].

2.1.1 Airway structure

Airways have a fractal structure [Goldberger and West, 1987]. After trachea the bronchi subdivide further several times, and the smaller subdivisions of the bronchial tubes are called bronchioles. At the end of the airway tree are the pulmonary acini including respiratory bronchioles, alveolar ducts and air sacs or alveoli, that are the destination of inhaled air. A model of airway system is presented in figure 2.2.

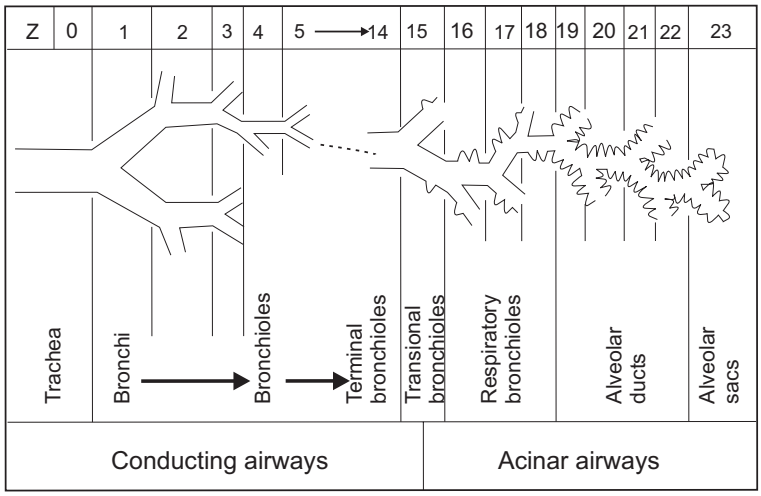

Fig. 2.2: Model of human airway system assigned to generations of symmetric branching from trachea to acinar airways, ending in alveolar sacs. Adapted from [Weibel, 1963].

In bronchi and large bronchioles (generations 2-11), the tube diameter is comparatively large, and to prevent collapse as the lungs expand, it is necessary to add some stiffness. This is the role of the cartilage plates, which decrease in size as the caliber of the bronchi does. Below a diameter of about 0.5 mm (in humans), the bronchiole walls contain only smooth muscle as a reinforcement.

2.1.2 Pulmonary acinus

Pulmonary acinus (respiratory unit) is defined as the zone including respiratory bronchioles, alveolar ducts and air sacs or alveoli. In human lungs this corresponds the generations 15-23, but the number of generations in a single acinus is quite variable. A human lung contains about 30000 acini, each with a diameter of 3.6 mm and containing about 10000 alveoli. The alveoli are the final branchings of the respiratory tree and act as the primary gas exchange units of the lung. The gas-blood barrier between the alveolar space and the pulmonary

capillaries is extremely thin, allowing for rapid gas exchange. To reach the blood, oxygen diffuses through the alveolar epithelium according to pressure gradient, and carbon dioxide follows the reverse course to reach the alveoli from the blood.

Distribution of the acini volume have a log-normal shape. This is due to irregular branching of the alveoli in the pulmonary acini (Figure 2.3). The gas flow in the airways is a sequence of redistributions at each airway bifurcation. When the probabilities of gas redistribution in a given bifurcation are not 50/50, such a process leads to the log-normal distribution of ventilation. These distributions are very common in nature [Rodriguez et al., 1987] and [Limpert et al., 2001].

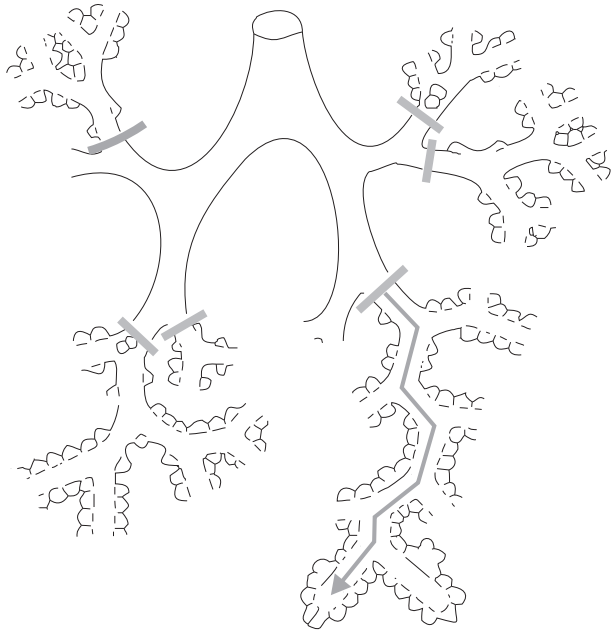

Fig. 2.3: Pulmonary acini are defined as originating at transitional bronchiole (marked by a cross bar) where the first alveoli appear. Figure adapted from [Haefeli-Bleuer and Weibel, 1988].

2.1.3 Gas exchange

Blood vessels around the walls of the alveoli are capillaries. Blood passes through the capillaries, brought to them by the pulmonary artery and taken away by the pulmonary vein. While in the capillaries the blood assigns carbon dioxide through the capillary wall into the alveoli and takes up oxygen from the air in the alveoli (figure 2.4). Differences between inspired and expired air are presented in table 2.1.

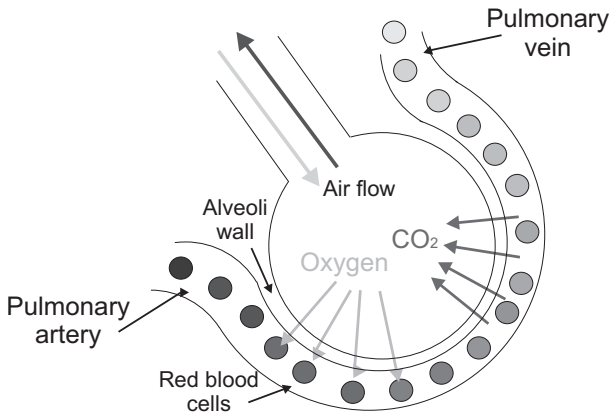

Fig. 2.4: Alveoli function

	Inspired Air	**Expired air**
Oxygen	About 21 %	About 16.4 %
Carbon Dioxide	About 0.03 %	About 4.0 %
Nitrogen	About 78.0 %	About 78.0 %
Water Vapour	Variable (rarely saturated)	Saturated
Temperature	Variable	About body temperature
Dust Particles	Variable but usually present	Little if any

Tab. 2.1: Composition of inhaled and exhaled air

2.1.4 Pulmonary circulation

The principal function of the lung is to exchange oxygen and carbon dioxide between blood and inspired air. Blood vessels in the lungs have a structure similar to the bronchial tree. Pulmonary artery carries de-oxygenated blood from the right ventricle to the lungs. Pulmonary artery branches first to the left and right lung and branches further down to the capillary level. The pulmonary veins carry blood from the lungs to the left atrium of the heart. They have inverse structure compared to the pulmonary artery, starting on the capillary level and reaching the main pulmonary vein which leads to the heart.

Gas exchange is dependent on local matching of regional ventilation-to-perfusion ratio ($\dot{V}_A/\dot{Q}$), where $\dot{V}_A$ is the alveolar ventilation and $\dot{Q}$ the perfusion. In normal lung, $\dot{V}_A/\dot{Q}$ is in balance regionally to provide an effective gas exchange. In lung disorders, $\dot{V}_A/\dot{Q}$ is often mismatched.

2.2 Modeling of lung function

2.2.1 Lung volume

Lung volume changes during ventilation. Figure 2.5 presents the change in lung volume during normal ventilation at rest and after a deep inspiration and expiration. Total lung capacity (TLC) is the volume of gas in the lungs after a maximal inspiration. Residual volume (RV) is the remaining volume after a maximal expiration. Functional residual capacity (FRC) is the lung volume after a tidal expiration.

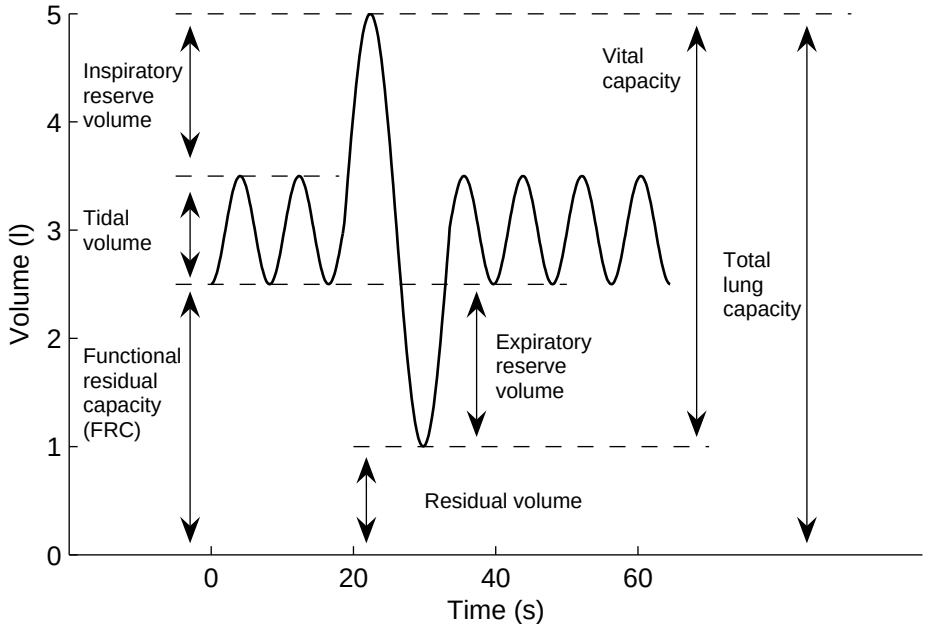

Fig. 2.5: Static volumes of human lungs. The spirometer curve indicates the lung volumes. Tidal volume, inspiratory reserve volume, expiratory reserve volume and vital capacity can be measured with a simple spirometry. The residual volume, total lung capacity and functional residual capacity cannot be measured without further elaboration of methods. Adapted from [Lumb, 2000].

2.2.2 Gas flow and resistance

The most important inspiratory muscle is the diaphragm. The movement of diaphragm causes pressure differences and changes the volume of the lungs. During inspiration, constriction of the diaphragm muscle fibres results a downward

movement of diaphragm and decreased pressure causes air to flow in the lungs. Normal expiration requires no muscle activation. When the diaphragm relaxes, elastic forces of the lungs and airway walls cause elastic recoil pressure and the air flows out of the lungs according to the pressure difference.

In airways the flow can be laminar, turbulent, or a combination of the two (transitional). When air flows at higher velocities, especially through an airway with irregular walls, the flow is turbulent and is found mainly in the largest airways, like the trachea. When the velocity is low and goes through narrow tubes, flow is laminar. Laminar flow is the most efficient way for oxygen transport to the distal parts of the bronchial tree. The total effective cross sectional area of the airways increases with each division of the airways from the trachea to bronchi, so that the flow rate of inspired gas falls. As the flow rate drops, the flow becomes rather laminar than turbulent. The transition between convection and diffusion depends on the morphometric properties of the airways. At smallest bronchioli level (generations 15-18) the gas transport changes from convection to diffusion and gas exchange in the alveoli [Lumb, 2000], and [Weibel et al., 2005].

Pressure difference in the airways causes gas to flow. Flow is the time derivative of the volume, (dV/dt), and in medical literature the flow is usually marked by $\dot{V}$. Volume flow dV/dt in a circular tube is calculated from equation

$$dV/dt = 2\pi \int_0^r v(r')\ r'\ dr', \tag{2.1}$$

where $v(r')$ is the velocity of the gas and r is the radius of the tube. In many problems the variations in velocity over the cross-sectional area A can be neglected and assumed to be constant and equal to the mean velocity $\overline{v}$ [Bentley, 1995]. Therefore

$$dV/dt = \pi r^2\ \overline{v} = A\ \overline{v}. \tag{2.2}$$

Airway resistance R is a local characteristic of gas flow in the lungs. It is defined as the ratio of driving pressure Δp to the gas flow dV/dt,

$$R = \frac{\Delta p}{dV/dt} = \frac{\Delta p}{A\overline{v}}\ , \tag{2.3}$$

where Δp is the pressure difference. The unit of resistance R is [Pa·s/m^3]. Resistance in the airways depends on whether the flow is laminar or turbulent, on the dimensions of the airway, and on the viscosity of the gas. For laminar flow, resistance is quite low and relatively small driving pressure is needed to

produce a certain flow rate. Resistance during laminar flow may be calculated from Poiseuille's Law:

$$R = \frac{8l\eta}{\pi r^4} \tag{2.4}$$

where l is the length of the tube, η [Ns/m^2] the viscosity of the gas and r the radius of the tube [Lumb, 2000]. Evidently, the tube radius r has a large impact on resistance.

For turbulent flow, resistance is relatively large compared with laminar flow, so that a much larger driving pressure would be required to produce the same flow. Pressure-flow relationship is not linear during turbulent flow, and direct calculation of the resistance is complex.

While a single small airway provides more resistance than a single large airway, resistance to air flow depends on the number of parallel airways present. For this reason, the large and particularly the medium-sized airways actually provide greater resistance to flow than do the more numerous small airways. Airway resistance decreases as lung volume increases because the airway diameters increases as the lungs inflate, and have lower resistance. The total airway cross-sectional area and the resistance at different airway generations are presented in figure 2.6.

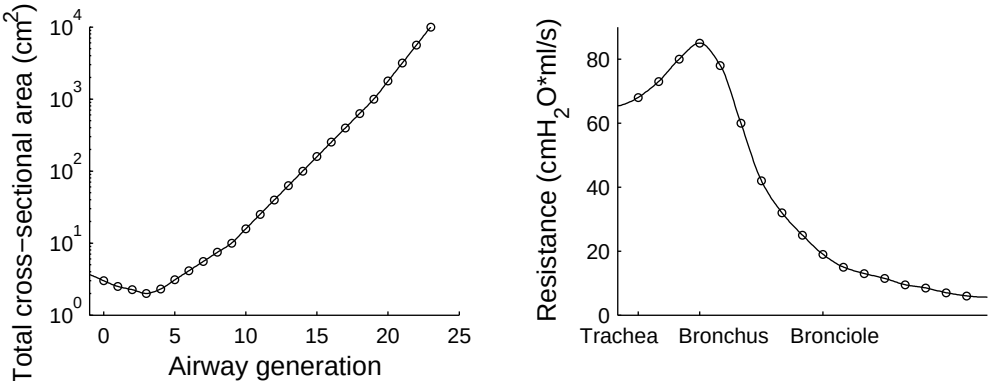

Fig. 2.6: The total airway cross-sectional area of the airways at different generations of airways is presented in the left figure. The total cross-sectional area becomes very large in the small airways approaching a square meter in the alveolar ducts in humans . The right figure presents the airway resistance as function of airway generation (figure adapted from [Lumb, 2000]).

2.2.3 Ventilation

When a single compartment is filled by inhalation (or emptied by exhalation), the driving pressure is proportional to the unfilled volume $V_{as} - V$, where V_{as} is the asymptotic volume of the compartment. If the resistance R is constant, it is obtained from equation 2.3

$$dV = \frac{V_{as}}{\tau}(1 - \frac{V}{V_{as}})dt \ , \tag{2.5}$$

where τ is a characteristic filling (or emptying) time. The solution for the differential equation is of the form

$$V(t) = V_{as}[1 - e^{-(t-t_0)/\tau}] \ , \tag{2.6}$$

where t_0 is the arrival (exit) time and τ is identified as the time constant of ventilation. Specific ventilation $s\dot{V}$ is defined by the initial flow divided by the asymptotic volume V_{as}:

$$s\dot{V} = \frac{1}{V_{as}} \left(\frac{dV}{dt} \right)_{t=t_0} = \frac{1}{\tau} \ . \tag{2.7}$$

$s\dot{V}$ is a local parameter of lung function and it is used extensively in this work. Studies of $s\dot{V}$ are useful in medical research, because the results obtained with different imaging methods can be compared.

Obstructive diseases like asthma causes a delay of ventilation, i.e. τ is increased. In restrictive diseases the total lung capacity (TLC), and V_{as} are decreased [Sovijärvi et al., 2003]. Ventilation curves from one breath from normal, obstructive and restrictive cases are presented in figure 2.7.

2.2.4 Multiple breath models

When imaging with marker gas, a single breath may not give enough signal to visualize the ventilation. Therefore ventilation needs to be studied using multiple breath models. Single breath model can be extended to multiple breath models, because the multiple breath is a combination of several single breaths.

Multiple breath models are common in lung function research. They give direct information about the regional ventilation efficiency. The method is sensitive, and reveals even small changes in ventilation. The method is based on imaging the gas flow in inhalation (wash-in) or exhalation (wash-out). With a

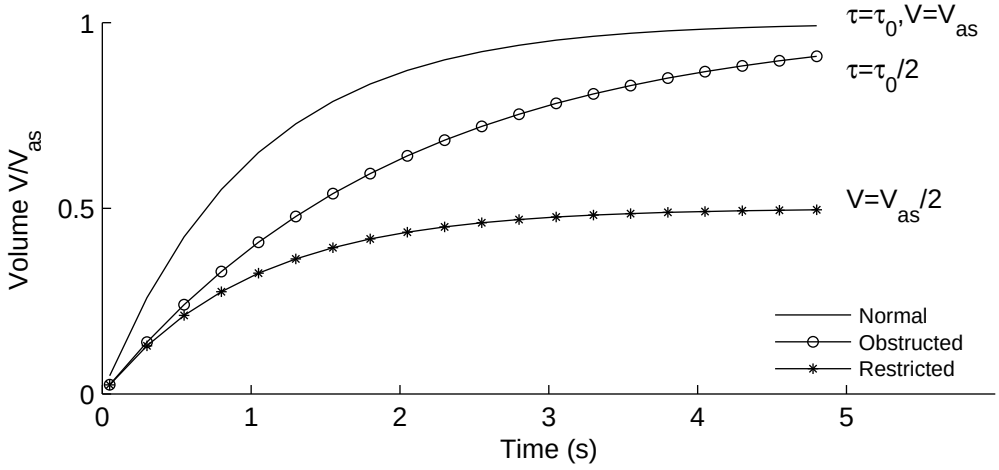

Fig. 2.7: Ventilation volume in normal, obstructed and restricted lungs. In obstructed case τ is increased. In restricted case V_{as}, or FVC is decreased.

marker gas and position sensitive imaging techniques changes in the local density can be followed and the local $s\dot{V}$ calculated. A wash-in and wash-out sequence is presented in figure 2.8.

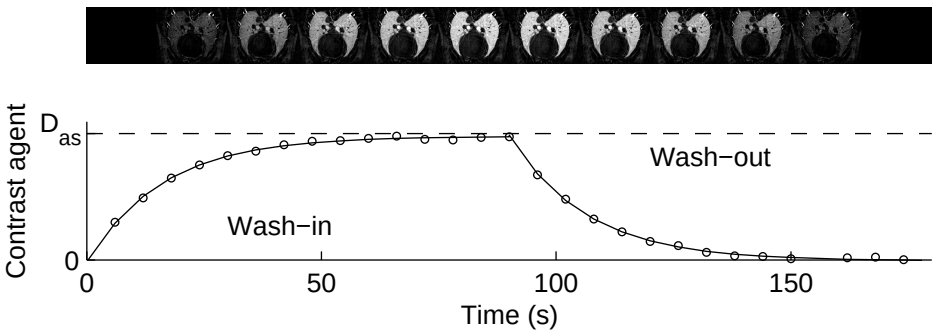

Fig. 2.8: Wash-in and wash-out sequences. In a wash-in sequence, the lungs are gradually filled with marker gas. In a wash-out sequence, the marker gas is flushed out from the lungs.

The change in the density due the marker gas or contrast agent in the wash-in or wash out sequence is usually described by mono-exponential dynamics using one-compartment model [Tajik et al., 2002]. A common way to calculate τ is to assume that it is equal for wash-in and wash-out series [Simon et al., 1998]. However, there may be differences in local τ for a wash-in and wash-out series [Chon et al., 2005]. It is also possible to take account the diffusion of the marker gas in the blood compartment using a two-compartment model [Kreck et al., 2001].

The local τ of a wash-in or wash-out sequence in one compartment model is calculated by fitting a function to the observed density. For a wash-in sequence the density of the contrast agent is

$$D(t) = D_{as}(1 - e^{-(t-t_0)/\tau}). \tag{2.8}$$

And for a wash-out sequence:

$$D(t) = D_{as}(e^{-(t-t_0)/\tau}). \tag{2.9}$$

Here D_{as} is the asymptotic density and τ is the time constant. The arrival time t_0 includes the transfer time from the gas valve to the trachea, and the transfer time from the trachea to the alveoli.

Multiple breath techniques have been used widely in imaging with using xenon-enhanced CT studies [Kreck et al., 2001], in positron emission imaging (PET) studies [Venegas et al., 2005b], and in magnetic resonance imaging (MRI) studies [Viallon et al., 1999].

2.2.5 Fractal analysis of ventilation distribution

A fractal structure or fractal process can be defined as having a characteristic form that remains constant over a magnitude of scales. A structure is fractal, if its small-scale form appears in its large-scale form. This property is called self-similarity, or the scale independence. The object needs not to exhibit exactly the same structure at all scales, but the same type of structures must appear on all scales [Mandelbrot, 1983].

The Koch curve (figure 2.9) created by mathematician von Koch in 1904, is a fractal structure that provides a simple introduction to the concepts of self-similarity and fractal dimensions. In the first generation it is a straight line with a length of l_0, in the second generation, the middle third of the line is replaced with two segments of lengths of 1/3 l_0. And this procedure is repeated until infinity.

The apparent length of the curve $L(l)$ depends on the length l of the chosen measuring device. If the line is divided in to N pieces, the relationship between the number of the pieces N, and measuring length l is obtained from the equation

$$l = l_0 N^{-(1/D)} \ , \tag{2.10}$$

where D is called the fractal dimension, and it gives information how the next generation is formed from the previous one. N can be expressed as

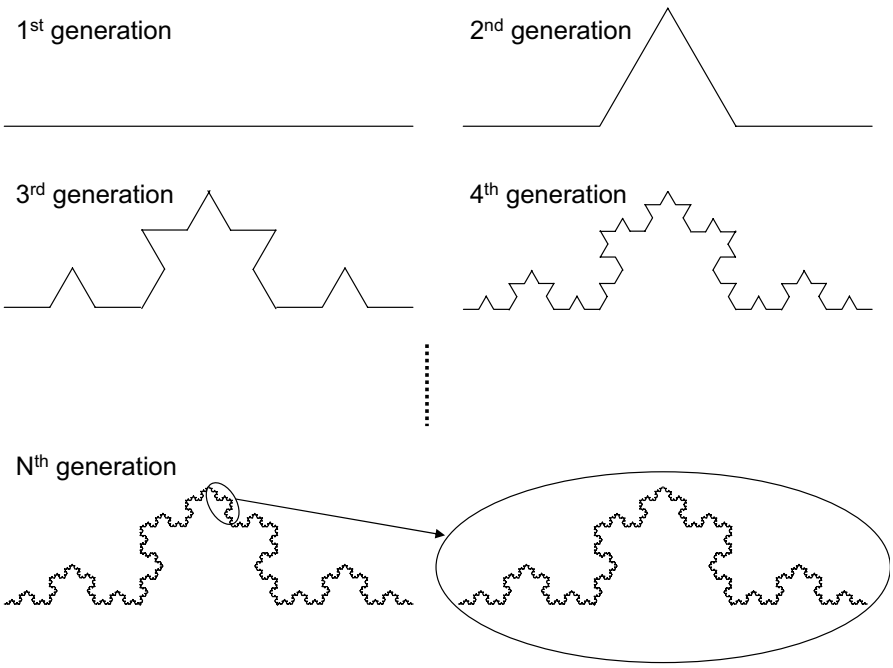

Fig. 2.9: Generation of the Koch curve produced by a simple iterative transformation, beginning with a straight line (1st generation). At each generation the middle part is replaced by 2 segments. Completed curve has an infinite number of iterations. Regardless of magnification of scale, any part of the curve resembles the whole curve.

$$N = \frac{L(l)/l}{L(l_0)/l_0} = \frac{L(l)}{L(l_0)}\frac{l_0}{l} \ . \tag{2.11}$$

Combining these two equations, we obtain

$$\frac{l}{l_0} = \left(\frac{L(l)}{L(l_0)}\frac{l_0}{l}\right)^{-(1/D)} \Rightarrow \left(\frac{l}{l_0}\right)^{-D} = \frac{L(l)}{L(l_0)}\frac{l_0}{l} \Rightarrow \left(\frac{l}{l_0}\right)^{1-D} = \frac{L(l)}{L(l_0)} \ . \tag{2.12}$$

Taking the logarithm of both sides and rearranging the terms yields

$$\ln L(l) = (1-D)ln(l/l_0) + \ln L(l_0) \ . \tag{2.13}$$

In this form, a log-log plot of $L(l)$ vs. l/l_0 produces a line with a slope of $(1-D)$. In the description of potential fractal structures in nature, Mandelbrot described a simple rectangular branching algorithm of the airways in bronchial

tree [Mandelbrot, 1983]. The structure of the bronchial tree is fractal down to acini level, but at that level the structure changes and the self-similarity disappears [Altemeier et al., 2000].

In studies of the distribution of ventilation, parameter used for fractal analysis is the heterogeneity in ventilation as a function of the size of the considered region of interest (ROI) with a volume of V. The heterogeneity of ventilation is calculated by the coefficient of variation CV [Bassingthwaighte, 1988] and [Glenny and Robertson, 1990]. The fractal dimension D for CV can be calculated from equation

$$\ln CV(V) = (1 - D) \ln \frac{V}{V_0} + \ln(CV(V_0)) \ , \tag{2.14}$$

where CV(V) is the CV of ventilation at a regional volume V, and V_0 is the voxel volume. Therefore, D can be calculated from a linear fit from a log-log plot of CV(V) vs. V/V_0.

When V is large, CV follows a straight line. On the acini level V becomes small enough that the alveolar gas pressure becomes uniform. The volume of this region, termed the unit of ventilation (UV) is identified by a change in the slope of CV (Figure 2.10) [Altemeier et al., 2000].

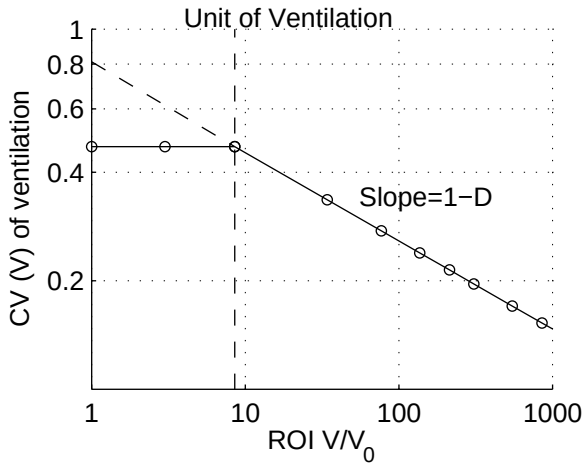

Fig. 2.10: A theoretical fractal plot of ventilation demonstrates no further increase in heterogeneity below certain cluster limit size. This point is termed the unit of ventilation (UV). Figure adapted from [Altemeier et al., 2000].

2.3 Methods for lung function studies

2.3.1 Experimental studies of ventilation distributions

The measurement of regional pulmonary ventilation is important in studies of lung physiology and investigations of lung disease. The measurement of lung ventilation has traditionally been made for the entire lung, despite the fact that lung function in both health and disease is inhomogeneous [Marcucci et al., 2001]. Early imaging studies of local ventilation distribution were performed with scintigraphic methods [Ball et al., 1962], and [Milic-Emili et al., 1966]. Later studies of the distribution of ventilation have been performed with microspheres [Altemeier et al., 2000], with xenon-enhanced CT [Kreck et al., 2001], with positron emission tomography (PET) [Vidal Melo et al., 2003], and with magnetic resonance (MRI) [Spector et al., 2004].

2.3.2 Spirometry

Spirometry is the most basic and frequently performed test of pulmonary function. A device called spirometer is used to measure air flow dynamics and lung volumes during maximal ventilatory maneuvers. Because spirometry is based on a maximal forced inhalation or exhalation, the accuracy of its results are highly dependent on the patient's understanding, co-operation, and best efforts. Most commonly used measured variables are forced vital capacity (FVC) and FEV1, which is the forced expiratory volume in one second [Sovijärvi et al., 2003].

2.3.3 Scintigraphic imaging methods

Clinically, ventilation imaging has been performed by use of radionuclide scintigraphic techniques, including radioactive gases, radiolabeled aerosols, and positron emission tomography with positron-labeled gases, but these methods have limited spatial and temporal resolution, and they are not quantitative [Cho et al., 1993] and [Gefter, 2002].

Radiospirometry is a method where the ventilation is studied by inhaled radioactive gases. Imaging is performed with extra-thoracic gamma detectors, and the distributions of ventilation, lung volumes and perfusion can be measured. The gases used are xenon (Xe^{133}) krypton (Kr^{81}) and different aerosols marked with technetium (Tc^{99}) [Sovijärvi et al., 2003]. Gamma cameras are the most common imaging devices in the hospital, and this imaging method is widely used in clinical lung studies, usually combined with pulmonary perfusion studies [Milic-Emili et al., 1966] and [Sovijarvi et al., 1982].

Single photon emission computed tomography (SPECT) provides computed tomographic images of the 3D distribution of radioisotopes in the body. Positron emission tomography (PET) is a functional imaging method based on the detection of radiation from the annihilation of positrons. marker gases are short lived positron emitters, such as nitrogen (N^{13}), oxygen (O^{15}) and fluorine (F^{18}). The resolution of the animal PET system is approximately 1.5 mm, whereas the resolution of the clinical PET system is approximately 5 mm [Tai and Laforest, 2005]. SPECT and PET are widely used in clinical studies. PET can be used also for determination of the ventilation perfusion ratio [Treppo et al., 1997].

PET/CT device is a combination of a PET scanner and x-ray CT scanner. PET/CT device can provide both anatomic information and functional information in a single imaging session as well as accurate registration of PET and CT data. In a PET/CT scan, a helical CT scan is normally performed before the PET scan to obtain a CT image to provide anatomic information. Motion artifacts are possible, because the PET and CT images are not taken simultaneously, even if they are taken with the same scanner. The spatial resolution of CT is in order of 1 mm, and 5 mm for PET [Pan et al., 2005].

2.3.4 Magnetic resonance imaging with hyperpolarized gases

Magnetic resonance imaging (MRI) has been established as the imaging modality of choice in many regions of the body. Magnetic resonance imaging of the lung, especially functional imaging of pulmonary ventilation represent great challenges since the low proton spin polarization within the lungs results in a low signal-to-noise ratio, cardiac and respiratory motion have to be compensated, and considerable susceptibility gradients arising from the air and tissue interfaces produce a very short T2-relaxation. Some of these difficulties may be overcome by MRI based on the use of hyperpolarized noble gases [Middleton et al., 1995] and [Moller et al., 2002]. Most common marker gases for lung studies are helium (He^3) [Kauczor, 2003], xenon (Xe^{129}) [Oros and Shah, 2004], and fluorene (F^{19}) [Ruiz-Cabello et al., 2005]. Another method for the assessment of regional ventilation by MRI is the use of oxygen for signal enhancement [Hatabu et al., 2001]. The signal from paramagnetic O_2 is far inferior to that from spin-polarized He^3, but the method is less complex and provides clinically useful information [Johnson and Hedlund, 1996]. The time resolution is excellent. Spatial resolution with human MRI is in order of 1 mm/pixel and the slice thickness is several millimeters. However, with high-resolution MRI scanners for small animals, the pixel size is in order of 100 μm, and the slice thickness 500 μm [Benveniste and Blackband, 2002]. MRI is only a semi-quantitative method, and the exact amount of the marker gas is difficult to estimate. Although magnetic

resonance imaging avoids the concern about ionizing radiation, there is insufficient signal from airway walls to visualize anything but the largest airways [Brown and Mitzner, 2003].

2.3.5 Xenon-enhanced CT

Xenon-enhanced computed tomography (Xe-CT) is a technique for the noninvasive measurement of stable xenon gas in the lungs with conventional x-ray CT scanners [Gur et al., 1979], and [Gur et al., 1981]. Xenon is a strongly absorbing gas, and the relative densities of xenon in the CT images can be calculated. The method is not quantitative, but when imaged in a conventional CT scanner, the density of xenon measured in Hounsfield units (HU) increases linearly with its concentration in the lungs [Marcucci et al., 2001]. Typically the gas mixtures used as contrast agent contain 30-60% of xenon. Wash-in and wash-out time constants determined from serial computed tomography scans are used to study the regional pulmonary ventilation [Simon et al., 1998]. The resolution is typically 1 cm^3, but with high-resolution CT scanners it is possible to obtain higher resolutions [Gefter, 2002]. The time resolution is adequate for functional studies, but the noise is relatively large compared to the signal from the contrast gas. Xenon is most used gas in X-ray CT studies, however recent studies shows that ventilation can be studied also without contrast agents [Guerrero et al., 2006].

2.3.6 Fluorescent microspheres

Fluorescent microsphere (FMS) aerosol technique is a method which gives high resolution estimates for distributions of ventilation and pulmonary blood flow [Zeltner et al., 1991]. It is possible to use different sizes of inhaled fluorescent microspheres (FMS) with different fluorescent labels at the same time, and study the pulmonary blood flow by intravenous injection of the fluorescent microspheres simultaneously. Typically the microsphere sizes are 1.0-μm diameter in ventilation studies and 15.0-μm in pulmonary blood flow studies. After the administration of the fluorescent microspheres, the animal is euthanized and the lungs are extracted and cut to small pieces. The ventilation and blood flow maps are calculated from the fluorescent signals of the pieces [Melsom et al., 1997].

2.3.7 Experimental studies of airway narrowing

Asthma is a condition characterized by eosinophilic inflammation of the bronchial mucosa airway, which results in reversible increases in bronchial smooth muscle tone. During an acute asthma attack, the airways narrow due to bronchospasm,

which leads to increased airway resistance. Because of the increased smooth muscle tone during an asthma attack, the airways also tend to close at abnormally high lung volumes, trapping air behind occluded or narrowed small airways. In research, airway narrowing and broncho-constriction is induced by irritating drugs, such as histamine and methacholine.

In vitro studies of broncho-constriction are performed with a video microscopy using precision-cut lung slices [Martin et al., 1996]. With this method airways are cut into thin (220 μm) lung slices. Constriction of airways is observed under a microscope, which in combination with video microscopy and digital imaging techniques makes it possible to visualize and quantify broncho-constriction. The smallest airways that we have been able to analyze by this technique have a diameter of only 50 μm, corresponding roughly to the terminal bronchioles Both ovalbumin and methacholine produce a broncho-constriction in precision-cut lung slices, and both dose-response studies and kinetic studies have been done [Dandurand et al., 1993] and [Wohlsen et al., 2001]. A major advantage of these techniques is that airways of all generations can be studied with little limitation in image resolution. On the other hand, central nervous system and circulatory influences are absent, and the load on airway smooth muscle is theoretically smaller in isolated than in intact lung [Wohlsen et al., 2003].

Although other imaging modalities have potential to see into the lungs, most of the *in vivo* studies of broncho-constriction have been performed with high-resolution CT (HRCT). It is possible to study the airway narrowing by different routes, as aerosol, as injection and as local injection in the lungs [Petak et al., 1997], [Brown and Mitzner, 2003]. Airway narrowing is typically caused by a challenge of histamine [Brown et al., 1998], or methacholine [Amirav et al., 1993].

2.3.8 Structural and functional models

Theoretical studies in physiology generally make use of models that describe the physiological function, anatomic structure, or experimental result. A simple description with explicit assumptions allows one to examine a complex phenomenon, and to make predictions that are experimentally testable. Structural models of the branching ductal systems of an organ are useful for studying the correlation between structure and function. First models were one and two dimensional fractal structures proposing structural airway models that include airway dimensions and connectivity, and were symmetrical [Weibel, 1963]. Later the models take in account of the natural asymmetry in the lungs, because each terminal has a different pathway [Horsfield et al., 1971], and [Haefeli-Bleuer and Weibel, 1988]. These models have been extensively applied to the study of lung mechanics and gas exchange by adding a branching ratio [Horsfield, 1990] and flow diameter

relationship [Kitaoka and Suki, 1997], and fractal modeling [Glenny et al., 1991]. However, these models do not include information about the spatial arrangement of the airway structure, and hence they are limited to modeling lung function in two dimensions (2D). Therefore the development of 3D models of the airway and vascular branching systems has been growing recently [West et al., 1997], [Kitaoka et al., 1999], and [Mauroy et al., 2004]. Besides of airway dimensions and their spatial arrangement, modeling is applied to study gas mixing and distribution of ventilation [Paiva and Engel, 1987], pulmonary alveoli function [Paiva and Engel, 1984], [Sapoval et al., 2002], and [Kitaoka et al., 2000], and aerosol mixing [Darquenne and Paiva, 1994], and [Butler and Tsuda, 2005]. Recently the models have been adapted to study the airway narrowing and how the narrowing affects on the distribution of ventilation [Gillis and Lutchen, 1999] and [Venegas et al., 2005b].

3. AIMS OF THE STUDY

The purpose of the present study was to develop a new imaging method, where stable xenon gas is imaged within the airways and lungs with synchrotron radiation in 2D and 3D, and to use the method to investigate the lung function and structure. Lung function and structure were studied by imaging the ventilation distributions and airway sizes in healthy, mechanically ventilated and anaesthetized rabbits. Furthermore, airway narrowing by broncho-constriction was studied with healthy animals using histamine provocation.

Present work was designed to study following items:

- To develop a system for functional lung imaging to visualize stable xenon gas within the airways and lungs in 2D and in 3D
- To study the distributions of ventilation in 2D, the effect of tidal volume on the distribution of ventilation, and the fractal properties of the distribution of ventilation
- To perform 3D imaging of regional lung gas volume with spiral CT
- To study the kinetics of the airway narrowing, and changes in regional ventilation during histamine-induced broncho-constriction

4. MATERIALS AND METHODS

This chapter covers the materials and methods used in this thesis. A more detailed description is given in the respective original publications I-IV.

4.1 Pre-clinical and clinical research with synchrotron radiation

Ever since the X-rays were found, the application of ionizing radiation to the field of medicine has become increasingly important. The development of dedicated synchrotron radiation sources has allowed exciting advances in many of these applications. The new sources provide tunable, high-intensity monochromatic beams over a wide range of energies which can be tuned to specific needs. There are wide variety of medical applications in synchrotron radiation, from imaging methods to radiation therapy [Suortti and Thomlinson, 2003], [Lewis, 2004], and [Thomlinson et al., 2005].

Medical research is performed at several synchrotron radiation facilities around the world. The research field is expanding fast and the number of medical facilities is rising accordingly. Major research programs are conducted in the facilities, presented in table 4.1. All experiments presented in this thesis were performed at the European Synchrotron Radiation Facility (ESRF), in France.

4.2 Synchrotron radiation

Synchrotron radiation provides a source of monochromatic X-ray beams which are tunable over a broad energy range and well suited to *in vivo* medical imaging. In the following the characteristics of a synchrotron radiation source refer to the ESRF. Electrons emitted by an electron gun are first accelerated in a linear accelerator (linac) and then transmitted to a circular accelerator (booster synchrotron) where they are accelerated. These high-energy electrons are then injected into a large storage ring, where they circulate in a vacuum environment, at a constant energy, for many hours. Electron energy at ESRF is 6 GeV and the circumference of the storage ring is 844 m.

In Europe:	
Elettra	Trieste,Italy
European Synchrotron Radiation Facility (ESRF)	Grenoble, France
Synchrotron Radiation Source (SRS)	Daresbury, U.K
In USA:	
Advanced Light Source (ALS)	Berkeley, California
Advanced Photon Source (APS)	Argonne, Illinois
National Synchrotron Light Source (NSLS)	Brookhaven, New York
In Asia:	
Photon Factory	Tsukuba, Japan
Super Photon Ring - 8 GeV (SPring8)	Nishi-Harima, Japan

Tab. 4.1: Medical research at synchrotron radiation facilities.

The storage ring includes both straight and curved sections. As electrons travel round the ring, the electrons pass through different types of magnets. Bending magnets deflect the electrons from their straight path by several degrees. The storage ring at ESRF has 64 bending magnets to provide full 360^o turn. Focusing magnets, placed in the straight sections of the storage ring, are used to focus the electron beam to keep it small and well-defined. Synchrotron radiation is produced by the bending magnets, because the change in direction makes electrons to emit electromagnetic radiation. More powerful radiation is produced with high magnetic field insertion devices, undulators and wigglers [Als-Nielsen and McMorrow, 2001].

4.3 Contrast agent imaging with synchrotron radiation

Various subtraction methods can be used to detect contrast agents in a tissue. In general, two images are needed, with a difference in one of the variables, such as time or energy. These images are subtracted from each other to visualize the contrast agents against the background [Elleaume et al., 2002].

The temporal subtraction method can be used when the movements of the object do not blur the subtraction image. A reference image, taken without contrast agent, is subtracted from a set of images taken with contrast agent. Temporal subtraction has been used widely in imaging of blood vessels in the brain using iodine and gadolinium as contrast agents [Le Duc et al., 2000] and [Adam et al., 2003].

Dual-energy subtraction methods use two separated energies to image the sample, and take advantage of the energy dependence of the photoelectric effect.

Usually this is performed at the K-edge of the contrast agent and the method is called K-edge subtraction imaging (KES). The sharp rise of the attenuation coefficient at the K-edge energy provides a way to clearly identify this element among several others. Work in this thesis is based on the KES imaging method and the principles of KES are described in the next section.

4.3.1 K-edge subtraction imaging

The idea of imaging simultaneously with 2 beams was developed a long time ago [Jacobson, 1953], but it proved to be impossible to create monochromatic x-ray beams with sufficient flux from conventional x-ray tubes. The method became useful in the early 80's when synchrotron radiation became available for medical imaging and it was technically feasible to have beams for the imaging. Motion artifacts are largely eliminated in KES imaging, because the images are taken simultaneously [Elleaume et al., 1997]. There is no blurring caused by motion, but if the subject moves during imaging, structural distortions are possible.

KES imaging with synchrotron radiation was originally developed for human intravenous coronary angiography with iodine as contrast agent. The method has been used in human patients [Rubenstein et al., 1986], [Rubenstein et al., 1990], [Thomlinson, 1996], and [Elleaume et al., 2000]. Other possibility is to use gadolinium in the blood as contrast agent [Le Duc et al., 2000]. In imaging of airways and ventilation, stable xenon is used as contrast agent. The feasibility of imaging airways using stable xenon gas as the contrast agent has been demonstrated in [Article **I**], where experiments were performed with animals. First *in vivo* experiments were performed with a human subject [Giacomini et al., 1998].

Xenon was chosen as an inhaled contrast agent because it is a stable, non-radioactive, inert gas that is also used in clinical imaging [Dingley et al., 1999]. Xenon has an anaesthetic side effects. Anaesthetic side effects start with concentrations above 35% [Yonas et al., 1981], but this is not a problem in our studies, because the experiments are performed with anaesthetized animals. Since the higher density of xenon may itself affect homogeneity of ventilation [Engel, 1986], care was taken to administer the same inhaled xenon concentration in all experiments using accurate mass flow meters for xenon and oxygen.

4.3.2 Physics of K-edge subtraction imaging

KES allows the observation of small anatomic structures carrying a contrast agent, while removing practically all features due to other structures in the object [Ebashi et al., 1991]. Two simultaneous images are acquired at two slightly

different energies, above and below the K-edge of a contrast element such as xenon. The attenuation coefficient of xenon increases by a factor of 5.4 when the K-edge at 34.56 keV is crossed, while the attenuation coefficients of cortical bone and lung tissue change by 1.8 % and 0.9 % per 250 eV, respectively. Here 250 eV is the typical energy difference between the wavelength bands used for KES imaging. The attenuation coefficients of xenon, bone and tissue are presented in figure 4.1.

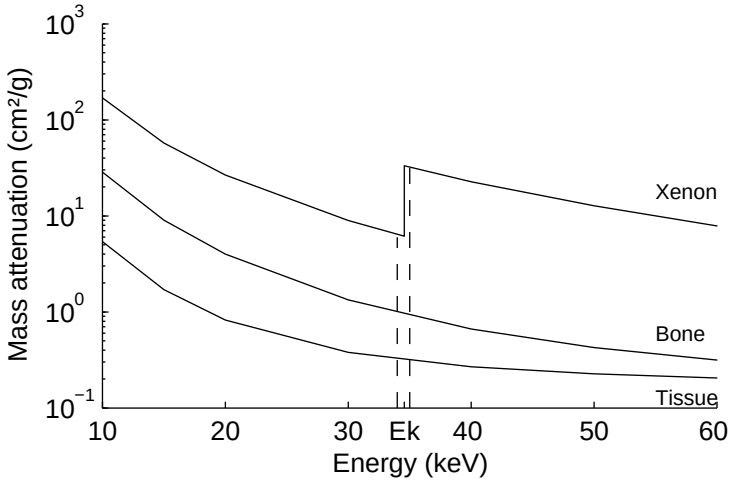

Fig. 4.1: Xenon attenuation coefficient compared to the attenuation coefficient of bone and tissue.

The attenuation of x-ray beam can be calculated from equation 4.1, where x is the length of the subject and μ is the absorption coefficient [Cullity, 1978],

$$I = I_0 \, e^{-\mu x} \ , \tag{4.1}$$

where I_0 is the intensity of the incident x-ray beam and I is the intensity of the transmitted beam. The absorption in an animal subject consists on the attenuation of the contrast agent (c), and the attenuation of tissue (t).

$$\ln\left(\frac{I}{I_0}\right) = -\mu \ x = -\left(\frac{\mu}{\rho}\right)_c \rho_c \ x - \left(\frac{\mu}{\rho}\right)_t \rho_t \ x \ , \tag{4.2}$$

where ρ is the density of matter and (μ/ρ) the mass attenuation coefficient.

$$\Delta\left[\ln\left(\frac{I}{I_0}\right)\right] = \ln\left(\frac{I_B}{I_0}\right) - \ln\left(\frac{I_A}{I_0}\right) = \Delta\left(\frac{\mu}{\rho}\right)_c \rho_c \ x + \Delta\left(\frac{\mu}{\rho}\right)_t \rho_t \ x \ , \tag{4.3}$$

where B notes the beam below the K-edge and A notes the energy above K-edge. The mass attenuation coefficient (μ/ρ) of xenon and tissue are presented in table 4.2.

μ/ρ [$\mathbf{cm^2/g}$]	$\mathbf{E < E_K}$	$\mathbf{E > E_K}$	$\mathbf{\Delta}(\mu/\rho)$
Xenon	6.13	33.16	27.03
Tissue	0.332	0.326	−0.006
Bone	1.044	1.011	−0.033

Tab. 4.2: The mass attenuation coefficients for xenon, tissue and bone) below and above the K-edge, and their differences [NIST, 2005]

Because the difference between the attenuation of tissue is negligible $\Delta(\frac{\mu}{\rho})_t \approx 0$, the equation 4.3 can be simplified to

$$\Delta\left[\ln\left(\frac{I}{I_0}\right)\right] = \Delta\left(\frac{\mu}{\rho}\right)_c \rho_c \, x \ . \tag{4.4}$$

In CT imaging the density of contrast agent ρ_c can be calculated directly from the subtraction image, because the pixel size is known. Figure 4.2 shows a KES CT image in mg/cm^3 units, and a single-energy image in Hounsfield units.

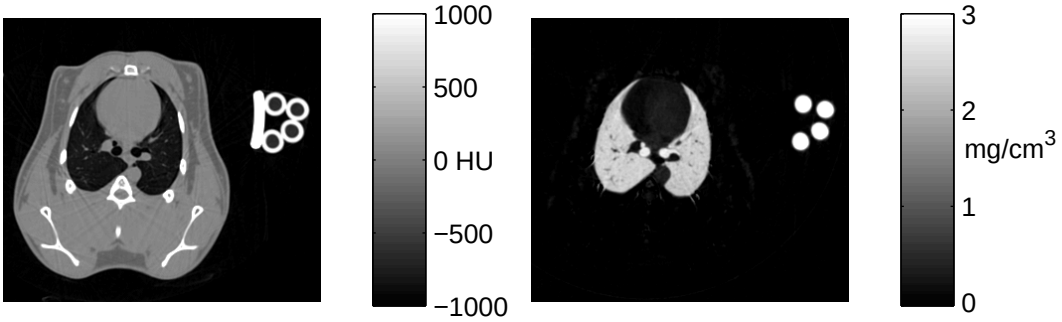

Fig. 4.2: Left: Absorption synchrotron radiation CT image recorded with one monochromatic beam in Hounsfield units. Plastic parts of the animal holder and tubing carrying xenon and oxygen to the animal are visible on the right to the animal. Right: K-edge subtraction (KES) image: only xenon-carrying structures like the airways, the lung tissue, and the tubing lumens are visible. The height of the image is 100 mm.

4.4 Medical beamline ID17 at ESRF

At the ESRF, one of the beamlines has been dedicated to medical applications of synchrotron radiation. The research program of the Medical Beamline (ID17) is the most extensive of all medical facilities, and it includes method developments, preclinical and clinical studies. The spectral flux of an X-ray beam produced by a synchrotron is thousand hundred times larger than that of the beam produced by a hospital X-ray scanner (figure 4.3) [Elleaume et al., 1999].

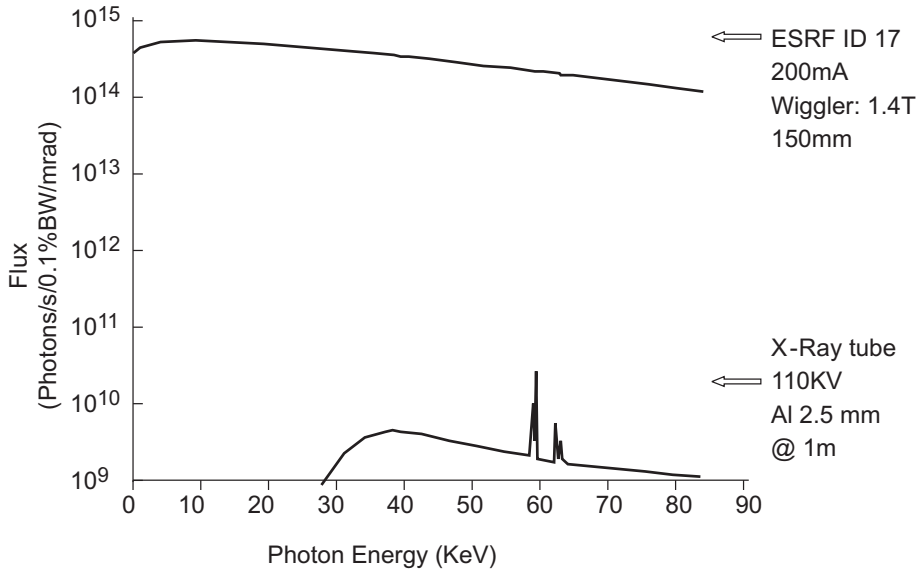

Fig. 4.3: Spectral flux of the beam available at the ESRF medical beamline compared to the flux available from a conventional tungsten X-ray source. Figure adapted from [Elleaume et al., 1997].

The facility consists of the x-ray beamline that delivers the high intensity x-ray beam from the storage ring source, associated optics and imaging detectors, and experiment hutches. Medical beamline has two experiment hutches. The first hutch is used in radiotherapy studies and it is close to the source in order to obtain the maximum X-ray intensity. The imaging takes place in a satellite building, which is located at 150 m from the source, where the beam is wider.

4.4.1 Source

The synchrotron radiation is produced in a 21-pole wiggler with a maximal magnetic field of 1.4 T. A wiggler is a magnetic structure, made up of an array of small permanent magnets, which forces the electrons to follow a wavy trajectory.

The beams of radiation emitted from the different bends overlap and add up to generate a much more intense beam of radiation than that generated by the bending magnets. In the present experiments a 60 mm magnet gap is used, and the wiggler field is 0.616 T, which corresponds to characteristic photon energy of 14.8 keV.

4.4.2 Beamline instrumentation

ID17 is a long beamline. The white beam reaching the imaging hutch is a fan with maximum dimensions of 300 mm width and 20 mm height. The beam is nearly parallel, because of the long distance from the source.

Optical components of medical beamline ID17 are presented in figure 4.4. The slits are used for limiting the beam, because in most of the cases only the center part of the beam is used. Beam monitors are ion chambers and they are used for on-line monitoring of the radiation dose. There are two monochromators, one for normal CT imaging and one for KES imaging which can be used alternatingly and the details are presented in next section. Imaging shutters are positioned after the monochromator and they are used during imaging, when the opening and closing of the beam is fast.

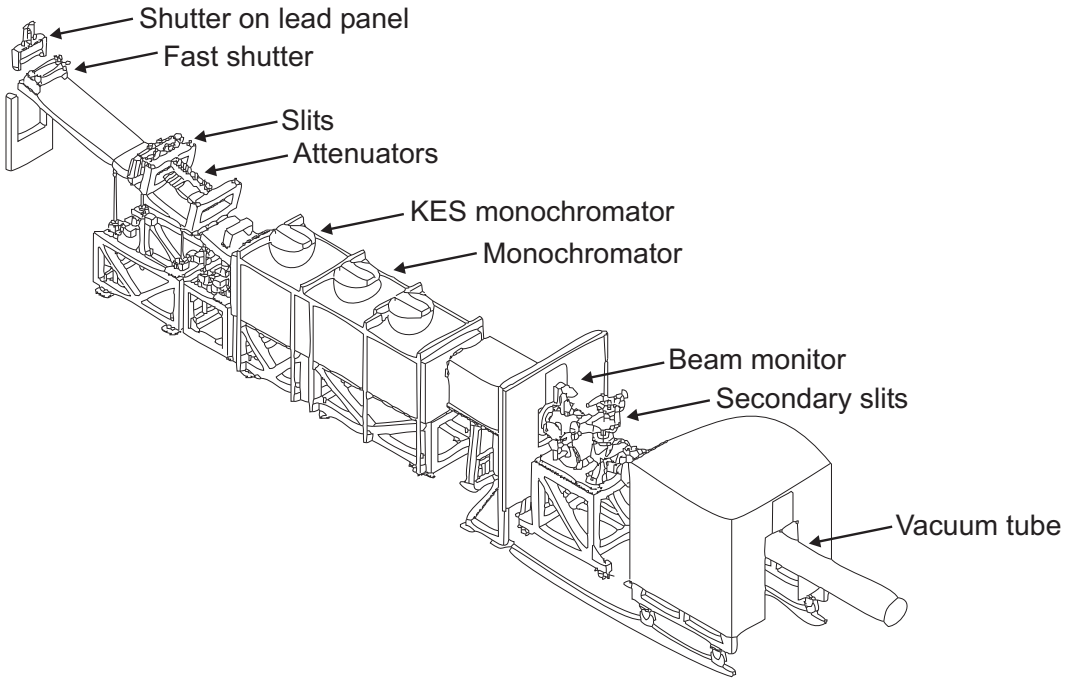

Fig. 4.4: Beamline optical components. Figure adapted from [Elleaume et al., 1999].

4.4.3 Monochromator

The experimental method used in this work is based on simultaneous imaging by two nearly monochromatic x-ray beams. These are produced from the continuous spectrum by a bent silicon crystal monochromator. The ESRF monochromator is a single cylindrically bent silicon (111) crystal in Laue geometry, which focuses the beam vertically [Suortti et al., 1993]. There is a vertical energy gradient, and the total energy bandwidth is 400 eV. Two nearly monochromatic beams are produced by cutting the middle part of the refracted beam after the monochromator, one beam with an energy above and the other below the K-absorption edge of the contrast agent. The beams have an energy bandwidth of 150 eV and their mean energies are separated by 250 eV. Monochromator and imaging setup are presented in figure 4.5.

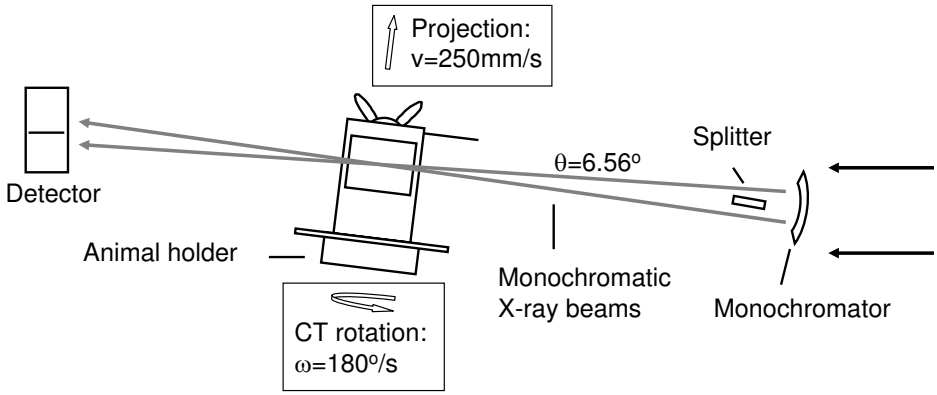

Fig. 4.5: Schematic picture of the imaging setup. Monochromator and splitter produce 2 nearly monochromatic beams for imaging. Beams focus and cross at the animal position and are recorded by a detector. During imaging the animal is rotated or scanned through the beams.

4.4.4 Scanning stage

Since the X-ray beam used in KES experiment is a stationary fan of about 0.7 mm in height and 150 mm in width, it is necessary to move or rotate the patient or animal through the beam.

The patient positioning system is a high precision stage with seven degrees of freedom. The stage allows both for positioning of the object and the scan motions during the data acquisition. It has high rigidity during rotation or translation. This is especially important for tomography, since any inaccuracy of the axis of rotation during the data acquisition will result in artifacts in the reconstructed

image. 3D computed tomography is made possible by acquisition of a large number of images during helical motion of the object.

4.4.5 Detector

In KES imaging, the two X-ray fan beams are recorded by a detector synchronously with the motion of the patient or animal. There are two different detectors at the Medical Beamline, a high-purity dual-line germanium detector (Ge) operating at liquid nitrogen temperature and a 2D FReLoN (Fast Read-out Low Noise) camera. Primary detector is the germanium detector. It is made from a monolithic P-type germanium crystal, width 150 mm and height 20 mm, electrically segmented into two rows of 432 parallel strips each (Eurisys Mesures). The thickness of the germanium crystal is 2.0 mm, giving an efficiency of nearly 100% at 34 keV. The major advantages of germanium detectors over other types of detectors are their very good efficiency together with a wide dynamic range [Peterzol et al., 2003]. In germanium, the photoelectric effect is the dominant attenuation process, and the mean-free path of the photo-electrons is small. The current produced by absorbed X-rays is measured directly with no amplification process. The 16-bit dynamic range of the electronics allows the measurement of signals over more than four decades. The spatial resolution of the system is determined by the vertical height of the beam and the 350 μm horizontal spacing of the elements on the detector [Elleaume et al., 1999]. A profile of the beams used in KES imaging and recorded with germanium detector are presented in figure 4.6.

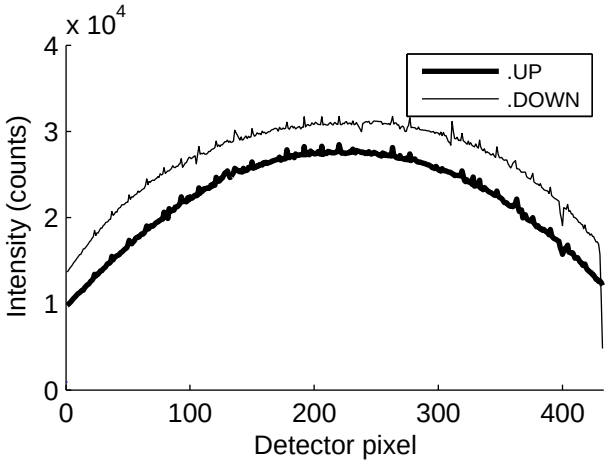

Fig. 4.6: 2 beams recorded with a 2 line germanium detector. 432 pixels in both lines, pixel width 350 μm.

The second detector at the medical beamline is a FReLoN camera. Frelon camera is a 100 mm x 100 mm 2D camera, with 2048x2048 pixels, giving spatial resolution of 50 μm pixel size [Bravin et al., 2003]. However, the dynamic range is lower and the read-out times are longer, so that the germanium detector is used in most of the KES studies.

4.5 *In vivo studies*

4.5.1 *Animal care*

Animal care and procedures of the experiment are in accordance with the Guidelines for the Care and Use of Animals provided by the American Physiological Society and approved by the local institutional authorities. The experiments are performed with rabbits (weight: 2.0-2.5 kg). To avoid movement artifacts in the images, the animals are anaesthetized, paralyzed, and mechanically ventilated. Anesthesia is induced by intravenous injection of thiopental sodium, and maintained with inhaled isoflurane. Paralysis is induced by IV pancuronium bromide. Because of the mechanical ventilation, the animal is tracheostomized with an endotracheal tube, which is connected to the mechanical ventilation system with a T-tube.

During histamine provocation the histamine aerosol is administered using an ultrasonic nebulizer. The mass median aerodynamic diameter (MMAD) of the aerosol particles is 3.5 m with a geometrical standard deviation of 2.0, according to the manufacturer. Typical histamine dose used in the experiment is a 125 mg/ml histamine solution in normal saline, administered continuously for 4 min.

4.5.2 *Mechanical ventilation*

During an experiment the animal is anaesthetized, and mechanical ventilation is used during the experiment. The goal is to create stable conditions for the experiment and an operation sequence that can be repeated many times during several hours to minimize the effect of short term variations and long-term drifting. The effects of short-term changes in lung shape and volume are minimized by pausing the ventilation during imaging (apnea). Moreover, mechanical ventilation gives the possibility to control and change the gas flow, depth of breaths (tidal volume) and respiration frequency.

Ventilation system consists of 2 different parts: the first one controls the gas mixture and the second one controls the inspiration and expiration valves. The system is remotely controlled by a computer and synchronized with imaging.

- Gas mixture control valves are directly connected to the gas bottles. Air, xenon (Xe) and oxygen (0_2) and their mixture are used. Gas flow is measured separately for each gas with mass-flow meters.

- Respiration gas control consists on inspiration and expiration valves. During inspiration the inspiration valve is open and the expiration valve is closed, and overpressure drives the gas in the lungs trough the T-tube. During expiration the expiration valve is open and the inspiration valve is closed, and lung relaxation releases the overpressure from the lungs trough the T-tube. During imaging both of the valves are closed, and the ventilation is paused at inspiration or at expiration. Mechanical ventilation causes inverted pressures compared to the spontaneous ventilation.

During resting period the animal breathes normally air, and during imaging a mixture of xenon and oxygen (volumes: 70 % / 30 %, respectively). Ventilation system is presented in figure 4.7.

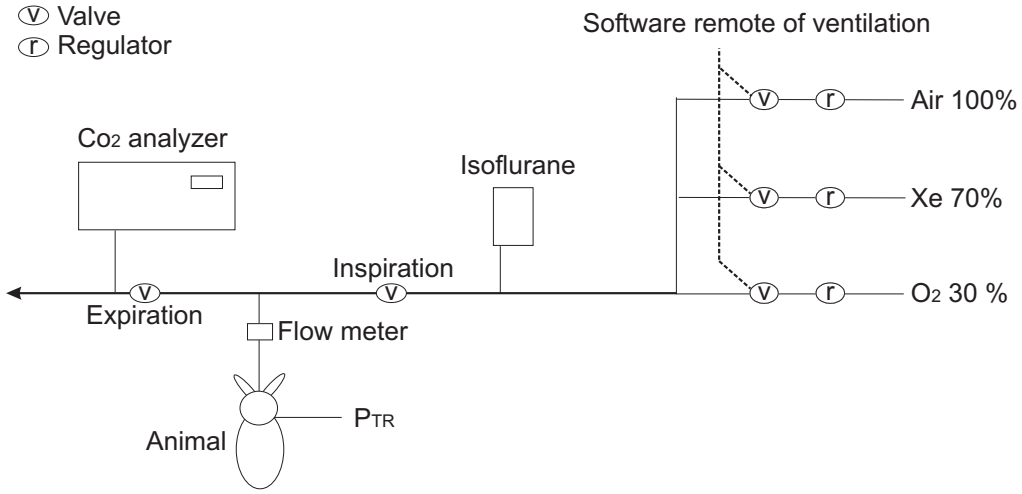

Fig. 4.7: Schematic presentation of the mechanical ventilation system. Ventilation is controlled by inspiration and expiration valves.

4.5.3 Physiological monitoring

Physiological parameters are followed up and recorded with a computer during the experiment. The gas flow is measured with a flow meter, and tracheal pressure P_{TR} and blood pressure P_A are measured with pressure sensors. Tidal volume (VT), and minute ventilation $\dot{V}$ are calculated from the flow. Carbon dioxide analyzer is used to measure carbon dioxide (CO_2) in the expired air. Figure 4.8

presents typical physiological parameters at baseline and after histamine provocation.

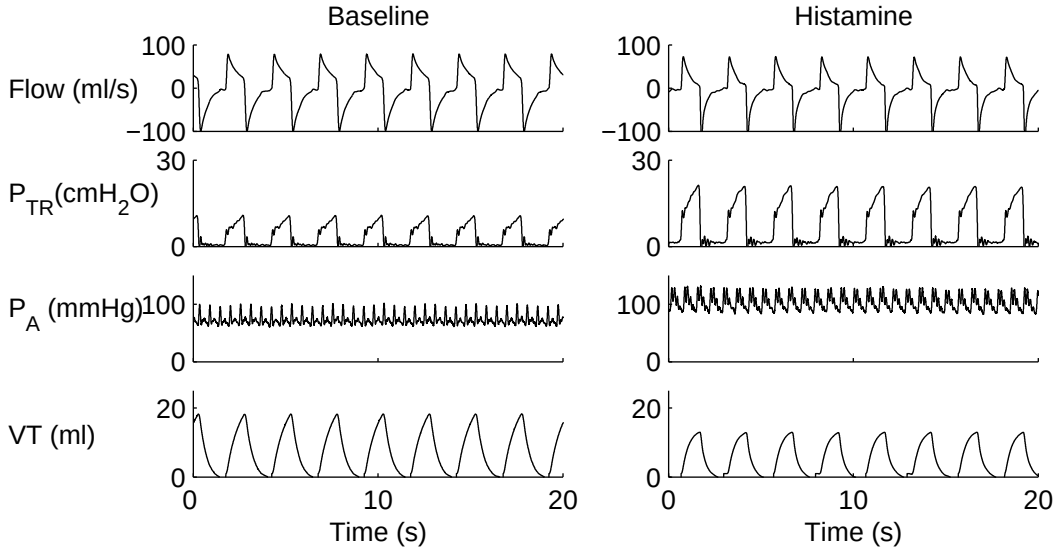

Fig. 4.8: Physiological monitoring at baseline and after histamine provocation. Histamine inhalation produces broncho-constriction, which increases P_{TR} and decreases VT.

4.6 Imaging

Because the beam is stationary, the animal has to be moved trough the beams during imaging. After the monochromator the beams are tilted upwards by 6.56^o. Maximum beam width on the animal position is 150 mm, limiting the maximum size of the animal.

4.6.1 Projection imaging

For projection imaging the animal is moved vertically through the fan beams. The detector is read out synchronously with the animal motion. Typical scan speed during imaging is 250 mm/s and the detector is read out every 1.4 ms. This results a projection image where the vertical pixel size is the same as the horizontal one, 0.35 mm.

4.6.2 CT imaging

For CT imaging the animal is rotated through the beam around an axis perpendicular to the fan beams. The detector is read out synchronously with the animal motion to provide 0.5^o angular resolution in the CT images. Typically the rotation speed is 180^o/s and images are recorded from 720 angular projections per full 360^o rotation. Projections from a whole turn form a sinogram. For quantitative imaging, the intensity distributions of the incident beam have to be measured prior to imaging. The center of rotation has to be stable during imaging. Changes in the center of rotation can be corrected in principle, but the reconstructed CT images may not correspond exactly to each other and may show artifacts, and data-analysis of many images may become complicated.

4.6.3 Spiral CT imaging

For spiral CT acquisition, the animal is rotated and moved vertically at the same time. Slice sinograms are interpolated from the continuous spiral sinogram data and reconstruction yields a 3D image of the subject. Typically the rotation speed is 360 ^{o}/s and the vertical velocity 1 mm/s. The pitch is defined as $P = st/w$ where s is the vertical displacement rate, w the beam thickness and t the revolution time. With a beam thickness of 700 μm, the pitch is 1.43, resulting in a slice thickness of 1.0 mm.

Spiral CT images are taken usually at Functional Residual Capacity (FRC) in order to minimize the artifacts caused by lung relaxation. In KES imaging the lungs are imaged in a steady-state density of xenon within the pulmonary alveoli. For minimizing the movement artifacts, the ventilation is paused during imaging. The apnea times are usually long, because several rotations are made during one apnea. Typically a 50 mm height image is recorded during an apnea of 55 s.

Spiral CT is a very useful and fast imaging method. However, long apnea times are not good for the animal, and cause changes in the shape of the lungs and the heart. It is necessary to make a compromise between the scan length and these artifacts in order to obtain good images.

4.6.4 CT reconstruction

Because the distance from source to the imaging room is large, 150 m, the beam is nearly parallel from object to the detector. Incident beam I_0 travels trough the object $f(x, y)$ and attenuates. The transmitted intensity I is a projection image of the object and it is recorded by the detector. The projection p_θ is the line integral of the attenuation coefficient $f(x, y)$ and rotation angle θ, as

illustrated in figure 4.9. The Fourier transform of the projection p_θ corresponds the data points of the fourier transform of the object $f(x, y)$ from the same angle θ [Kak and Slaney, 1988].

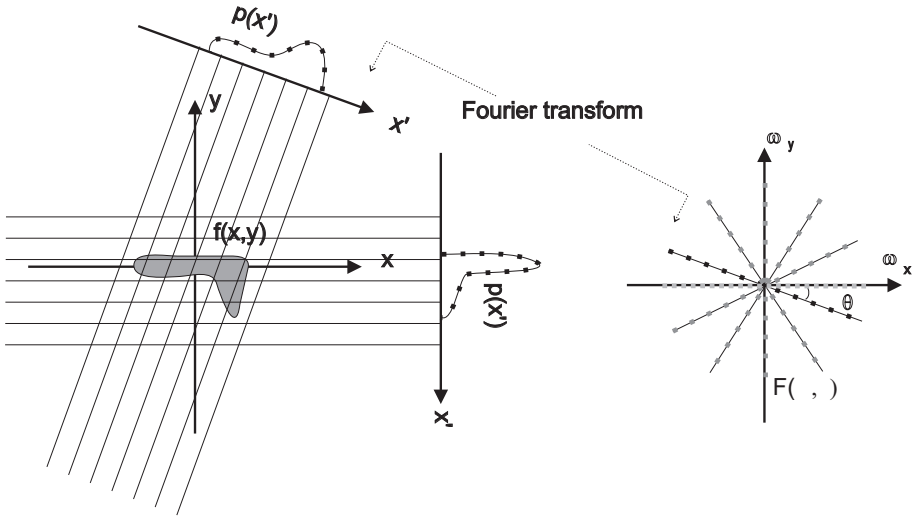

Fig. 4.9: Fourier slice theorem. The Fourier transform of $p(x')$ gives the line $F(\omega, \theta)$ from the Fourier transform of $f(x, y)$.

Reconstruction is performed with Filtered Back Projection. The method is based on Fourier Slice Theorem, where the projections are projected back to the image field at all imaging angles [Cho et al., 1993]. Because the projection data is discrete, the obtained data points in Fourier domain from object $f(x, y)$ are also discrete and in polar coordinates. Therefore there are less data points at larger frequencies, and the projections need to be filtered with high pass filter before the back projection. Filtered Back Projection is the most common reconstruction method.

After reconstruction of $f(x, y)$, the attenuation in the object is calculated at every square pixel. After subtraction in KES imaging, the signal comes only from the contrast gas, and the size of one pixel is known. Therefore it is possible to calculate the density of the contrast agent $\rho_c(x, y)$ at every pixel using equation 4.4.

4.6.5 Reconstruction artifacts

When imaging a living object, movements cause the most common imaging artifacts. In lung imaging the ventilation is paused during imaging, but the heart activity causes motion artifacts around the heart. Sharp edges, like bone, can

also cause imaging artifacts. These artifacts are a problem specially in subtraction imaging, if the 2 images are not taken perfectly at the same level. These two artifact types are difficult to correct for. Moreover, instrumentation may produce artifacts in the images. If all detector pixels are not working perfectly, the non-functional pixels cause ring artifacts in the CT image. However, it is possible to filter out these artifacts with a subsequent loss of resolution. Different types of artifacts are presented in figure 4.10.

Fig. 4.10: Artifacts from non-functional pixels, movements and sharp edges (bones).

4.7 Functional imaging

4.7.1 Multiple breath imaging

A wash-in imaging sequence starts by switching the inhaled gas from air to the Xe/O_2 mixture. Following a preset number of respiratory cycles, ventilation is paused for 3 to 4 seconds during which a tomographic image is acquired. The imaging cycle is repeated until an equilibrium density of xenon is reached in the lungs. Duration of wash-in imaging depends on ventilation, but usually this takes about 15 imaging cycles and the duration of an entire image sequence acquisition is 2.5 minutes. At the end of the imaging sequence inhaled gas is switched back to air.

In order to limit misregistration errors between images in a sequence, all CT images should to be obtained at the same level of lung inflation, usually after expiration at FRC. Imaging sequence and a wash-in image series are presented in figure 4.11. Cardiac gating is not possible to use, because the imaging times are long compared to the heart rate of the animal. However, the blur artifacts caused by cardiac motion on the sequential CT images are small.

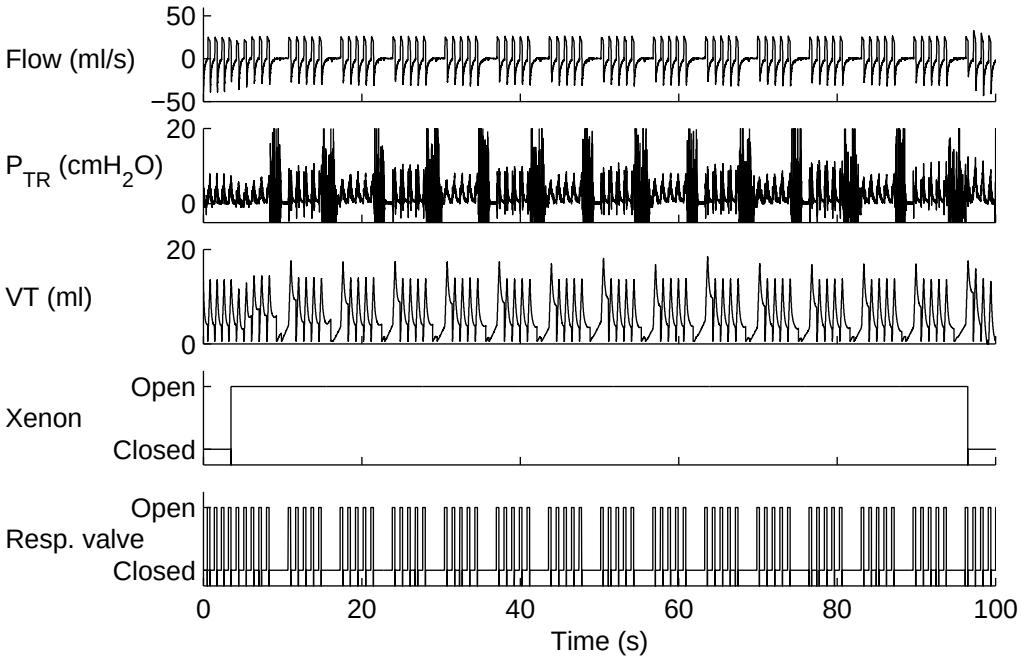

Fig. 4.11: Experimental wash-in imaging sequence. Gas flow, tracheal pressure (P_{TR}), tidal volume (VT) and xenon and respiration valve positions during imaging. Before the first image the ventilated gas is switched to Xe/O2 gas mixture. CT images are acquired during a breath-hold of 4.0 s. Between the images the animal breaths the gas mixture, until the equilibrium is reached in the lungs. At the end of the imaging sequence the inhaled gas is switched back to air. The rapid oscillations in P_{TR} are artifacts due to rotation of the animal.

The mathematics of multiple breath imaging is presented in section 2.2.4. Distribution of ventilation is calculated by fitting a mono exponential function to the wash-in curve. To minimize the effects of image registration errors in a wash-in series, a 5 x 5 pixel region of interest (ROI) is used for the fit, and major airways and blood vessels are excluded from the analysis. The instrumental resolution is 0.35 x 0.35 mm, but for the present smoothed maps of 1.75 x 1.75 mm resolution eliminate the effects of small differences in the animal position between the images.

Fractal analysis is based on the study of the heterogeneity in regional ventilation as a function of the size of the considered ROI. The coefficient of variation (CV) increases as the ROI size is reduced. Mono exponential function is fitted to the wash-in curve and regional ventilation as described earlier. Ventilation of distribution is calculated using ROI of 1 x 1 to 30 x 30 pixels, and CV is plotted as function of ROI. The variations in CV because of the exponential fit are estimated to be negligible, compared to the variations because of structural properties in the lungs.

4.7.2 Imaging regional lung gas volume

Regional lung gas volume is calculated from 3D images recorded by spiral CT [Monfraix, 2004]. A typical spiral CT acquisition sequence is presented in figure 4.12.

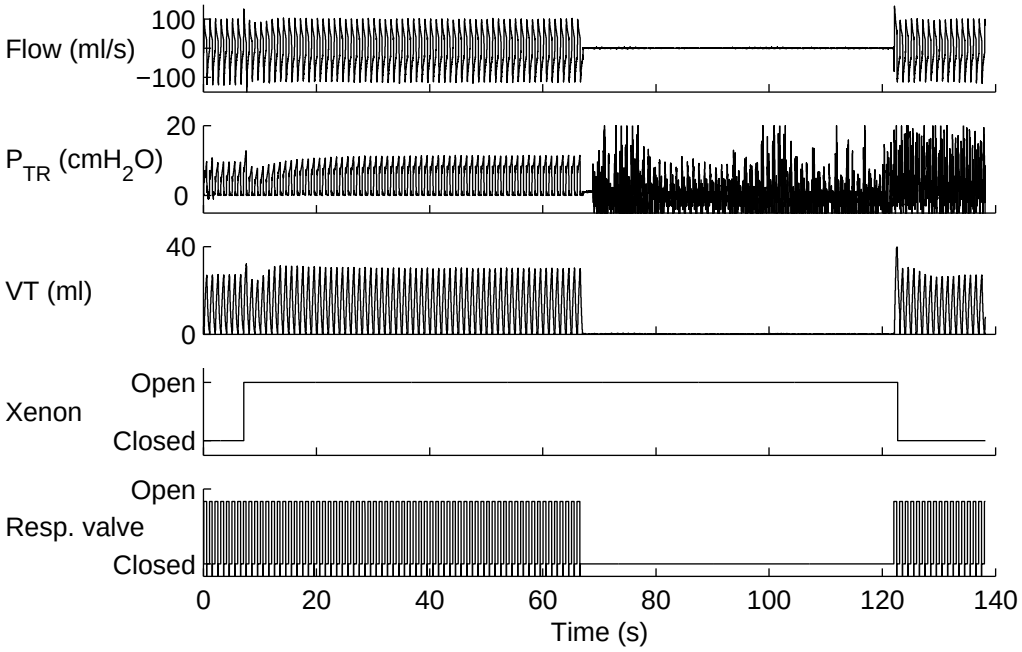

Fig. 4.12: Experimental sequence for 3D imaging with spiral CT. Before imaging, the animal breaths xenon and oxygen gas mixture until the equilibrium is reached in the lungs. Spiral acquisition is performed during a long apnea. Typically, 50 images are recorded during a 55 s apnea. Noise in the P_{TR} signal is due to the rotation.

A voxel of lung tissue consists of the tissue, blood and air space. Because the KES imaging method is quantitative, and the tissue and blood compartment are

subtracted away, the signal comes only from the xenon in the air spaces. Because the initial xenon gas mixture density is known, the regional lung gas volume can be calculated with an excellent resolution. Regional lung gas volume is measured from 3D spiral CT images. For a selected ROI in a reconstructed image, the local gas volume V_N is given by

$$V_N = V_v \sum_{i=1}^{N} \left(\frac{\rho_{Xe}}{D_{Xe}} \right) \ , \tag{4.5}$$

where N is the number of voxels contained in the ROI, V_v the volume of a single voxel, 0.35 x 0.35 x 1 mm^3 = 0.12 mm^3 (detector pixel size by slice thickness), ρ_{Xe} the measured xenon density and D_{Xe} the administered xenon density.

4.7.3 Imaging of broncho-constriction

During broncho-constriction the airway diameter decreases, and the distribution of ventilation changes. We developed a special imaging sequence to study the changes in airway sizes and ventilation distributions at the same time. The imaging sequence consists on 2 images, where first one is used to calculate the airway calibers, and the second one is used to study the ventilation. The experimental sequence for imaging airways and the distribution of ventilation is presented in figure 4.13.

The first image is taken a deep inspiration at approximately 70 % TLC estimated based on body weight [Takezawa et al., 1980] since the deep inspiration maximizes xenon density in proximal conducting airways. The luminal surface area of the airway is calculated from this image by fitting ellipses to contours of the xenon distribution in the airway, and airways whose diameters are larger that 2.0 mm can be measured accurately. The second image is taken after few ventilatory cycles in order to increase the alveolar density of the Xe/O_2 gas mixture at FRC, because the motion artifacts in the lung fields are minimal at end-expiration. The distribution of ventilation is measured from the area of xenon-filled airspaces in the lung fields from the second image. The area is called ventilated alveolar area, and typically xenon densities of mode ± 2SD are included.

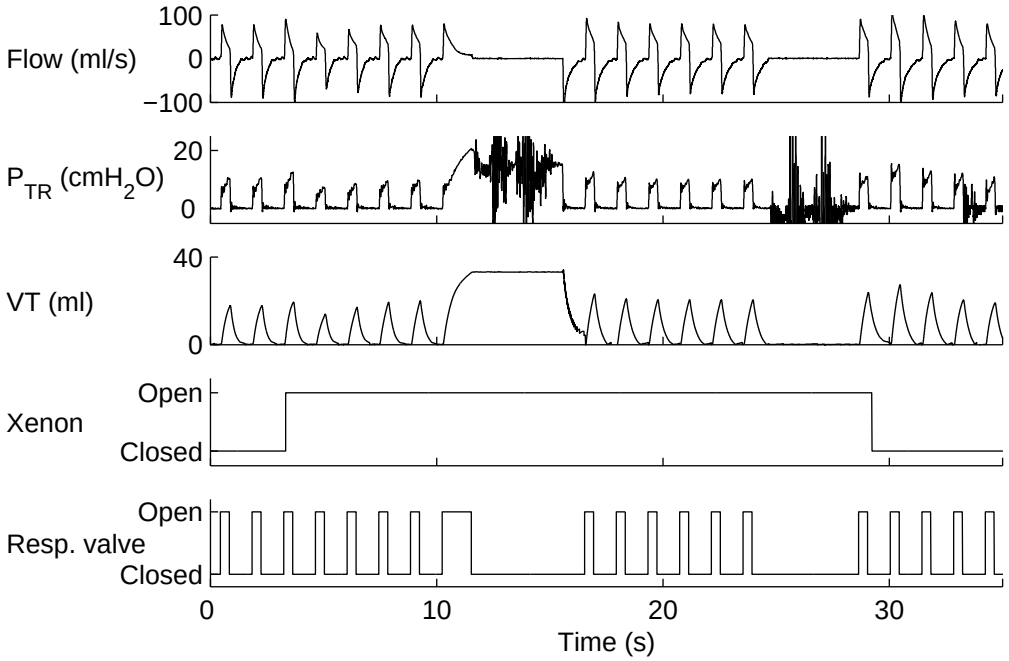

Fig. 4.13: Experimental sequence for imaging airways and the distribution of ventilation with CT. Before the first image the animal breaths 4 tidal ventilatory cycles of Xe/O_2 gas mixture followed by a deeper inspiration of 1.3 s. First CT image is acquired during a breath-hold of 4.0 s. After the first image, ventilation is resumed, and following 6 ventilatory cycles, second CT image is taken at end-expiration during a breath-hold of 4.0 s. At the end of the imaging sequence the inhaled gas is switched back to air. The rapid oscillations in P_{TR} are artifacts due to rotation of the animal.

4.8 Radiation dose

In medical imaging of humans and animals with synchrotron radiation, where the x-ray dose is a major issue, the energy should be higher than 30 keV to keep the entrance skin dose within an acceptable range [Elleaume et al., 2002].

The absorbed dose is calculated by absorbed energy per mass unit (Gray (J/kg)). The same absorbed dose delivered by different types of radiation may result in different degrees of biological damage to body tissues [Marttila, 1995]. The x-ray dose can be calculated from equation [Elleaume et al., 2002]

$$D = \Phi \left(\frac{\mu_{en}}{\rho} \right) E_\gamma \ , \tag{4.6}$$

where Φ is the photon flux [photons/m^2], μ_{en}/ρ the mass energy absorption coefficient of the object, and E_γ is the photon energy.

The x-ray dose delivered to the sample is derived from the germanium detector measurement. The number of photons N_0, incident on the detector per pixel, is given by

$$N_0 = e^{\mu_{Be} x_{Be}} \frac{N Q_{min} E_p}{E_\gamma \ (1 - e^{-(\mu_{Ge} x_{Ge})}) \ \overline{e} \ \text{gain}/128} \ , \tag{4.7}$$

where N is the detector reading (bits) in one pixel (typically 40000); Q_{min} is the minimum detectable charge ($Q_{min} = 2 \cdot 10^{-15}$ C); E_p is the mean energy necessary to create an electron-hole pair in germanium ($E_p = 2.98$ eV); "gain" is the electronic gain (from 1 to 128 with a factor of 2 between two consecutive gains, typically 4); ($E_\gamma = 34.56$ keV); μ_{Ge} is the total attenuation coefficient of germanium (1/cm); x_{Ge} is the detector thickness (0.2 cm) and $\overline{e}$ is the electron charge ($\overline{e} = 1.6 \cdot 10^{-19}$ C). The first term corresponds to the detector entrance beryllium window transmission factor (1 mm equivalent thickness, x_{Be}).

The photon fluence in time Φ_T (photons/s/m^2) can be calculated with equation

$$\Phi = \frac{N_0}{wh} \ \text{ and } \Phi_T = \frac{N_0}{wh \ dt} \ , \tag{4.8}$$

where the pixel width is $w = 0.35$ mm, the beam hieght is $h = 0.7$ mm , and the integration time of one line is $dt = 1.11$ ms. Typically we obtain a photon flux of $\Phi = 7.3 \cdot 10^6$ photons /mm^2 for one projection, and $\Phi_T = 6.6 \cdot 10^9$ photons/s/mm^2. The surface dose of a CT image of a cylindrical object can be calculated from equation

$$Dose = \Phi_T E_\gamma \left(\frac{\mu_{en}}{\rho} \right) \frac{t}{dt} \left[\frac{1}{2} + \frac{1}{2\pi} \int_{-\pi/2}^{\pi/2} e^{-\overline{\mu} r_o \cos\theta} d\theta \right] t \ , \tag{4.9}$$

here (μ_{en}/ρ) the mass energy absorption of tissue, $\overline{\mu}$ average attenuation coefficient, and r_o the diameter of the object (100 mm). Because acquisition time for one CT image is typically $t = 1.0$ s, we obtain a dose of 400 mGy for a KES dual-beam image pair [Ebashi et al., 1991], and [Elleaume et al., 2002]. In this study, no effort was made to minimize radiation dose. However, radiation dose delivered with synchrotron radiation sources is compatible with clinical application, and synchrotron radiation has been extensively tested in human patients for intravenous coronary angiography [Elleaume et al., 2000].

5. RESULTS

In this chapter the results of this thesis are summarized. The majority of figures is presented in the respective original publications I-IV.

5.1 Lung imaging with K-edge subtraction imaging

The first publication of this thesis, article **I**, demonstrated the feasibility of KES method at the European Synchrotron Radiation Facility. With KES imaging the airways and ventilation can be studied quantitatively, with excellent spatial resolution. Imaging of small airways down to 1.0 mm of diameter is possible. Method is sensitive, and even small chances in the ventilation can be measured. Fast imaging times makes functional studies possible. Figure 5.1 presents the first published KES projection images from a rabbit.

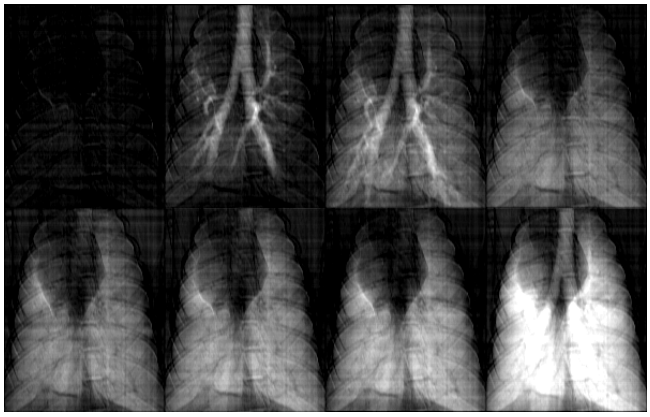

Fig. 5.1: A series of KES projection images starting at the switch of the inhaled gas from air to Xe/O_2. The actual size of one image field is 52.5 mm x 66.5 mm, and the time between the images 1.3 s. The imaging sequence was not synchronized to the respiratory cycle. The bronchial tree is visible down to the fourth bifurcation of approximately 1.0 mm in diameter.

5.2 Ventilation maps and uniformity

The second publication of this thesis (article **II**) presents the studies of ventilation in healthy rabbit, and the changes in the distribution of ventilation, when tidal volume (VT) is changed, but the minute ventilation was kept constant. Ventilation was measured with wash-in imaging sequence, the method is described in sections 2.2.3, and 2.2.4, and the imaging is described in section 4.7.1.

Figure 5.2 illustrates a series of specific ventilation ($s\dot{V}$) maps in one rabbit, obtained at the apical, middle, and basal lung levels, at 3 different VT's. These images demonstrate differences in regional ventilation, which were most apparent at the basal level of the lungs. Increasing VT without an increase in the minute ventilation increased the regional ventilation in all studied lung levels. The effect of VT on ventilation distribution is relevant to anaesthesia and intensive care.

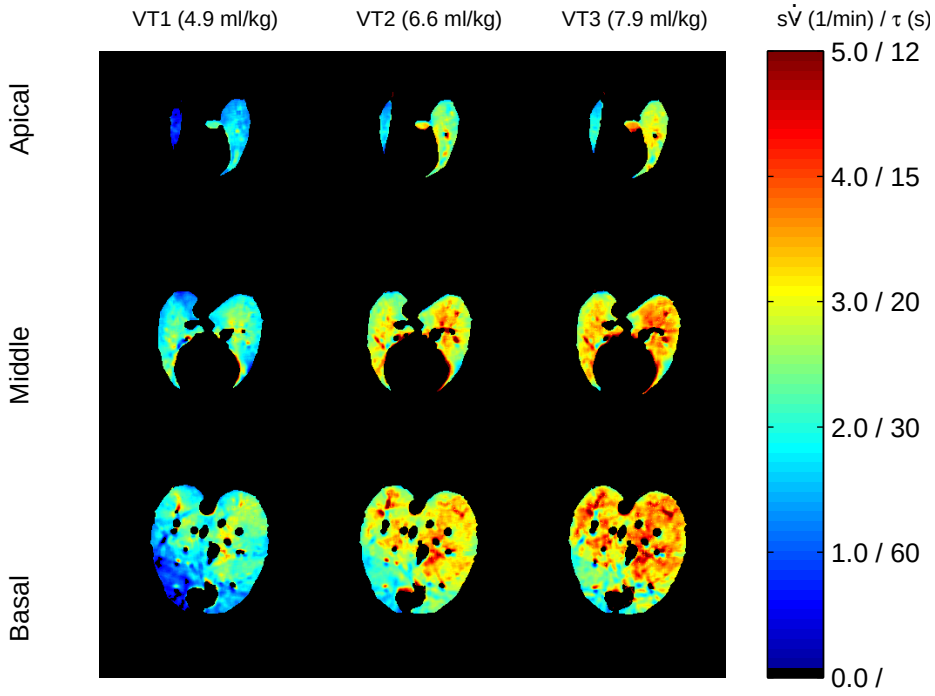

Fig. 5.2: Maps of $s\dot{V}$ and τ in one rabbit, obtained at apical, middle and basal lung levels, for 3 different VT (VT1, VT2 and VT3). The color scale is given in (1/min) and in (s), respectively. $s\dot{V}$ increased in all lung regions when VT increased. There was a significant difference in $s\dot{V}$ between dorsal and ventral areas at the basal lung level.

The distributions of time constant τ was found to be log-normal. The log-normal shape of the distributions may be explained by the fractal structure of the bronchial tree, which implies that the Xe/O_2 mixture reaches each position in the lung through a path that is characteristic of that position. When the probabilities of gas redistribution in a given bifurcation are not 50/50, a process leads to the log-normal distribution [Limpert et al., 2001]. Figure 5.3 shows frequency distributions of τ obtained from the same animal as in figure 5.2 at basal lung level. The histogram peak (τ max) shifted towards smaller values and the distribution became narrower when VT was increased. However, on the relative logarithmic scale, the width of the distribution remained nearly the same. The histograms are best described by the log-normal distribution [Majumdar et al., 2005]. This functional form is of fundamental importance for correct description of many statistical distributions met in nature [Limpert et al., 2001].

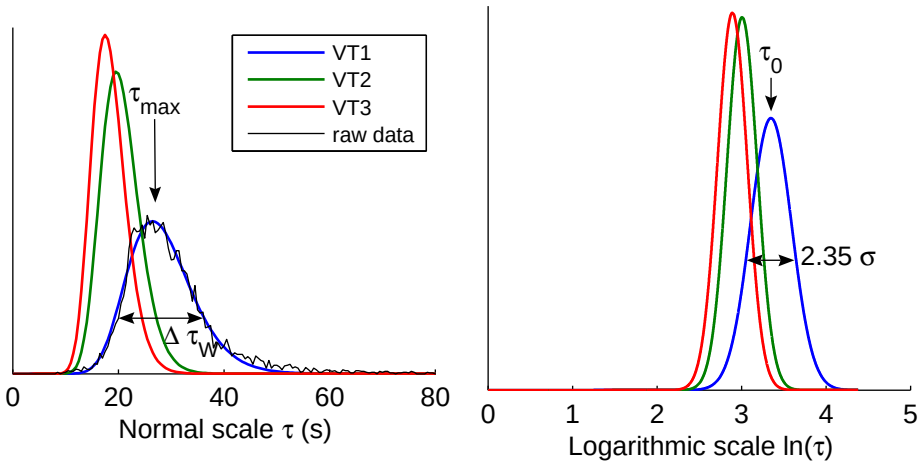

Fig. 5.3: Left: Histograms of xenon wash-in τ for one rabbit at at basal lung level for different VT in linear scale. The corresponding τ maps are presented in previous figure. Thin lines represent raw data, and log-normal fits are given by thick lines. The peak value τ_{max} and the full-width at half-maximum (FWHM) $\Delta\tau_w$ are indicated in one case. τ max and $\Delta\tau_w$ decreased when VT was increased. Right: Histograms of xenon wash-in τ(s) in logarithmic scale. The mean value $\log(\tau_0)$ decreased with τ_{max}, but the corresponding FWHM $= 2.35\ \sigma$ remained nearly constant.

5.3 Regional lung gas volume

In the third article of this thesis (article **III**) we have studied the regional lung gas volume, in normal conditions and after broncho-constriction, caused by inhaled histamine. The imaging sequence and analysis are presented in section 4.7.2.

The study demonstrates spiral KES-CT as a new technique for direct determination of regional lung gas volume, offering possibilities for non-invasive investigation of regional lung function and mechanics. An example of non-uniform volume distribution in rabbit lung following histamine inhalation is presented in figure 5.4. At the baseline, the ventilation is uniform. After histamine inhalation, the distribution became non-uniform, revealing poorly ventilated areas. On the other hand, the gas volume increased in some other areas. Regional respiratory system compliance was calculated from the regional lung gas volume at baseline, and it was found to increase with the distance from the lung apex.

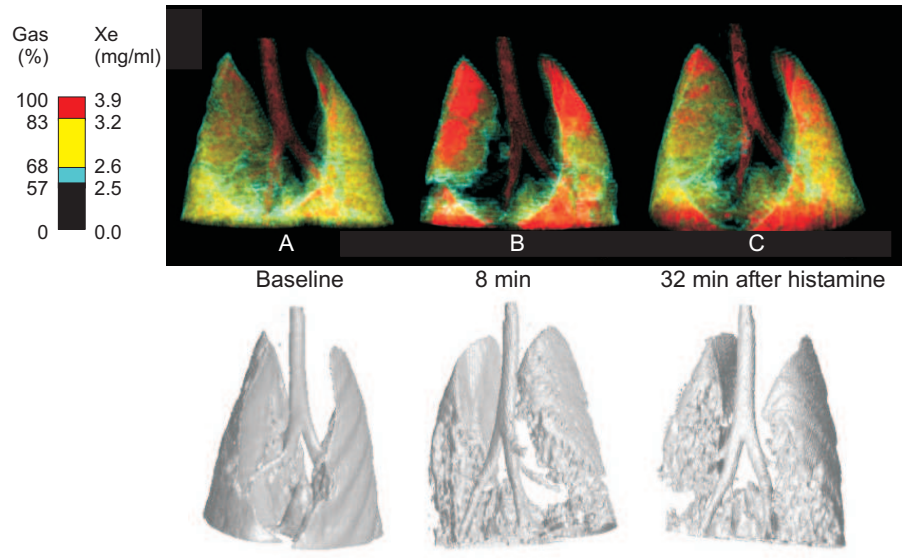

Fig. 5.4: Above: Volume-rendered 3D lung images, anterior view. Distribution of regional lung gas content is displayed using an artificial color scale, a: baseline, b: 8 min, and c: 32 min after histamine aerosol administration. The transparency of the lower end of the scale was reduced for better visualization of gas redistribution within the lungs following histamine administration. Below: Dorsal view of surface-rendered 3D lung images obtained in one rabbit at baseline and after histamine inhalation. Images 8 min after histamine inhalation show poorly ventilated areas, and after 32 min there has been recovery. Total image height is 49 mm.

5.4 Effects of histamine provocation in airways

The studies reported in the fourth article of this thesis (article **IV**) focus on kinetics of the changes in airway sizes and the homogeneity of ventilation during bronchoconstriction. More detailed description of animal models for studies of asthma is in section 2.3.7, and the experimental sequence in section 4.7.3.

Kinetics of histamine-induced broncho-constriction was studied up to 60 min after histamine inhalation in proximal and distal airways. The cross-sectional area of proximal airways was measured directly from the CT images, and distal airways were studied indirectly by measuring the effectively ventilated lung area. The results were compared using the respiratory system conductance. An example of the effect of histamine on proximal airway diameters in one animal are shown in figure 5.5. The luminal areas of proximal airways reached a minimum on the average 22 min after histamine provocation, and started to recover thereafter.

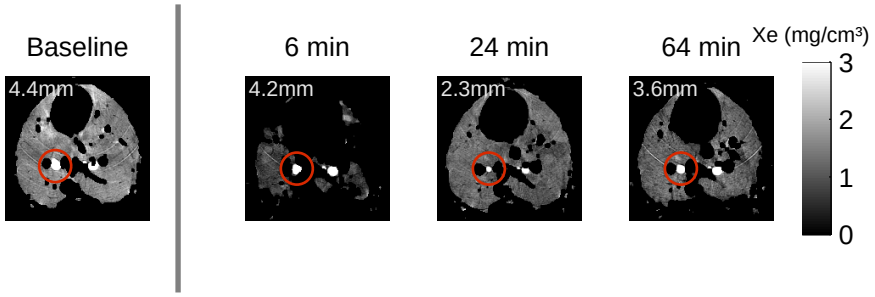

Fig. 5.5: Xenon distribution in the middle lung cross-section level at baseline and 6, 24 and 64 min after histamine inhalation in one rabbit. Changes in proximal airway caliber. The diameter of circled airway is marked in the upper corner of each image.

An example of the effect of histamine on distal airways in one animal are shown in figure 5.6. Distal airways reacted immediately to the histamine provocation, and started to recover thereafter. The histograms of ventilated alveolar area show unimodal distribution at baseline, but after histamine, the histograms were bimodal.

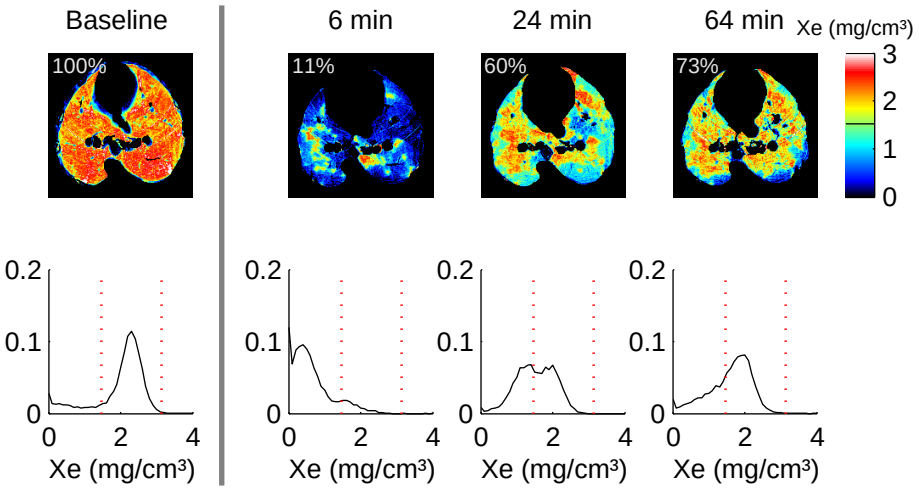

Fig. 5.6: Xenon distribution in the middle lung cross-section level at baseline and 6, 24 and 64 min after histamine inhalation in one rabbit. Above: changes in the ventilated alveolar area. Values are marked in the upper corner of each image. Below: Histograms of xenon density based on images presented above. Ventilated alveolar area was calculated based on the histograms by thresholding, density values within mode 2 ± SD were included (dotted lines).

The recovery of the distal airways was much faster than the recovery of the proximal airways. This is shown in figure 5.7. It is possible to fit simple functions to the observed data. Distal airway constriction and the conductance have a mono-exponential behavior, and proximal airway constriction has a bi-exponential behavior.

The curves describe the reaction to the histamine provocation. The initial drop in the ventilated alveolar area is not seen, because the reaction is almost immediate. Proximal airway behavior can be described with a bi-exponential equation: $f_1(t) = C(e^{-/(t-t_0)/\tau_1}) + (1 - e^{-/(t-t_0)/\tau_2})$. Distal airway behavior can be described with a mono-exponential equation: $f_2(t) = C(1 - e^{-/(t-t_0)/\tau})$. The time constant of the proximal airway reaction was estimated to be $\tau_{P1} = 8$ min. The time constants of spontaneous recovery for proximal and distal airways were $\tau_{P2} = 80$ min and $\tau_D = 10$ min, respectively.

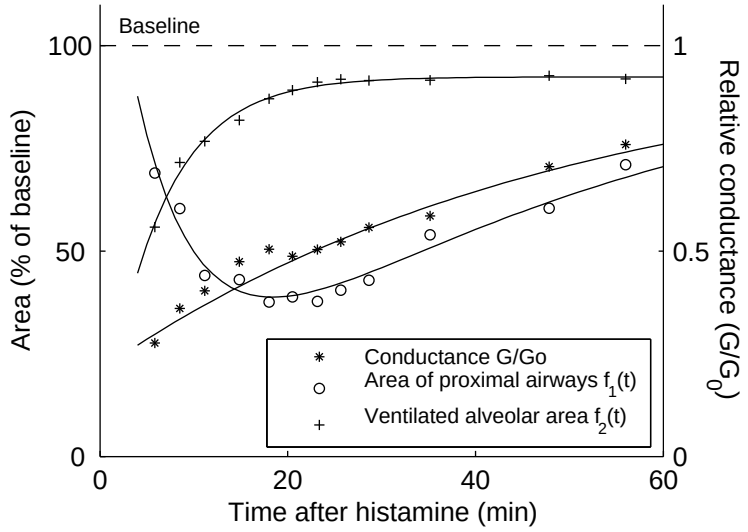

Fig. 5.7: Relative changes in overall respiratory system conductance relative to baseline (G/G_0), luminal area of proximal airways at the basal cross-section level where the largest response to histamine was observed (in % of baseline), and ventilated alveolar area after inhalation of histamine aerosol (in % of baseline).

5.5 Ventilation distributions and fractal analysis

Fractal analysis of ventilation was applied to the specific ventilation ($s\dot{V}$) maps measured in 5 healthy rabbits and presented in article **II**, but the present results were not included in that article. The theory of fractal analysis is explained in section 2.2.5. Ventilation was measured with wash-in imaging sequence, the method is described in sections 2.2.3, and 2.2.4, and the imaging is described in section 4.7.1.

Fractal analysis was performed by calculating the heterogeneity with the coefficient of variation CV of $s\dot{V}$ as function of studied region V (explained in figure 2.10) [Glenny et al., 1991]. Figure 5.8 shows a log-log plot the CV(V) of $s\dot{V}$. In logarithmic scale, the curve is linear when the volume of V is large, but when V becomes small enough, the increase in CV is not proportional to the change in the volume of V. The histograms of $s\dot{V}$ show that when V increases, the histogram becomes narrower. The variations in s$\dot{V}$ show the changes in anatomical structure. The variations in the calculation of s$\dot{V}$ are assumed to be negligible, because the calculation is very accurate [Porra et al., 2004].

Fractal dimension D and the unit of ventilation were calculated from 42 ventilation maps obtained from 5 different rabbits at 3 different lung levels in normal

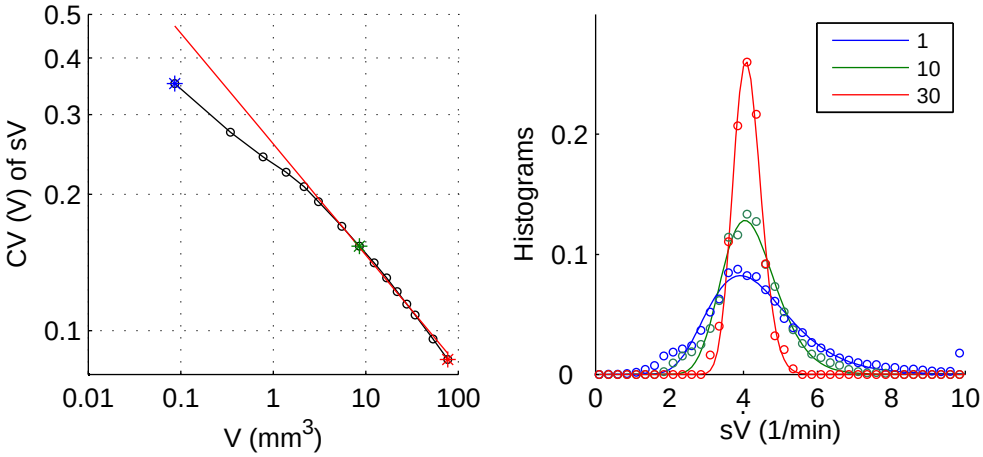

Fig. 5.8: Left: A fractal log-log plot of CV as function of V. Red line shows the linear plot of the slope, used in the calculation of fractal dimension D. Right: Histograms of $s\dot{V}$ shows how the distribution changes narrower, when V increases. The volume of V is $N^2 \cdot V_0$, when V_0 is the voxel volume and N=[1,10,and 30]. Figure shows the raw histograms and the log-normal fits of the histograms. The presented data is an example from one rabbit, in one imaging level.

conditions. Results are presented in table 5.1. Measured D values depend on the lung level. D was highest at the apical lung level and lowest at the basal lung level. The difference was significant between all imaged lung levels (P<0.01, Students t-test), indicating structural differences in the different areas of the lungs. A change in VT did not affect D. Values measured in this study were similar to those previously reported, D=1.15-1.20 in pigs although comparison is difficult because of different species [Altemeier et al., 2000]. Moreover, this analysis is performed to 2 dimensional CT images, and comparison with results obtained with 3D techniques is complicated.

	Apical	**Middle**	**Basal**	**All levels**
Mean	1.32	1.24	1.15	1.24
SD	0.09	0.06	0.08	0.10

Tab. 5.1: Fractal dimension D calculated at different lung levels.

Theoretically, the size of the unit of ventilation (UV) can be calculated from the change in the slope of log-log plot of CV(V). In our results the slope of CV(V) changes, but in most cases the exact location of the change is difficult to estimate. Moreover, the calculations are from 2-dimensional CT images, and that has an effect in the estimation of UV. So far, only theoretical estimations of

the size of UV have been possible. Based on our data, the size of UV is in the range of 2.0 mm^3-4.2 mm^3.

A more complete analysis of the results is underway, and the results will be published separately [Porra et al., 2006]. The analysis is being extended to images taken after histamine provocation. In particular the branching ratio of the airways may be determined from the shape of the log-normal distributions shown in figure 5.8 [Majumdar et al., 2005].

5.6 Statistical accuracy

Unlike CT with standard x-ray sources, the signal intensity on subtracted KES images depends only on xenon density. The results are totally independent of changes in the lung tissue density, resembling scintigraphic methods using radioactive xenon but with much higher spatial resolution.

A single energy image in Hounsfield units (HU) and a KES image are presented in figure 4.2. The signal to noise ratio (SNR) can be calculated for figure with equation

$$SNR = 10 \log \frac{\overline{\mu_S}^2}{\sigma_{BG}^2} , \tag{5.1}$$

where $\overline{\mu_S}$ is the mean signal in a region of interest (ROI), and σ_{BG} is the standard deviation of the background noise. In image analysis ROI is chosen to be an area where the values are similar. For lung image analysis we chose a 5x5 pixel area, and calculated for a single energy image SNR = 41 dB, and for a KES image SNR = 29 dB.

Small variations in the density of lung tissue have a large effect in multiple breath methods. In a single-energy CT, particularly at energies below xenon K-edge, absorption in xenon gives only a relatively small contribution to the total absorption in lung, and the statistical noise is seen as much larger deviations from the fitted curve than in the KES case. However, the use of an x-ray energy just above the K-edge enhances absorption in xenon, so that the radiographic density increases by more than $D_{as} - D_0 = 300$ HU between the final (D_{as}) and initial (D_0) densities of lung tissue and xenon. As an example, a fitted D(t) in a typical wash-in sequence in a KES image series and in a single energy transmission image series are shown in figure 5.9. The exponential fit to the observed xenon density D(t) is excellent in the KES case, but in a single energy series the noise is markedly larger. Mean normalized summed squared residuals (SSR) are normalized with the density change in a wash-in series, for comparison of the two curves. Mean

SSR was 10.8 % for a single energy image and 0.6 % for a KES image. These SSR values are slightly better than values published in article **II**, because the CT reconstruction has been developed, which improves the quality of image series. However, the relation in the accuracy between a single-energy image and a KES image stays similar. When the residuals in different methods are compared it must be taken account that they depend on the imaging protocol, the density of the inhaled gas, and the size of the used ROI. Moreover, it can be expected that the errors would be considerably larger for an image acquired using a broad-band x-ray source.

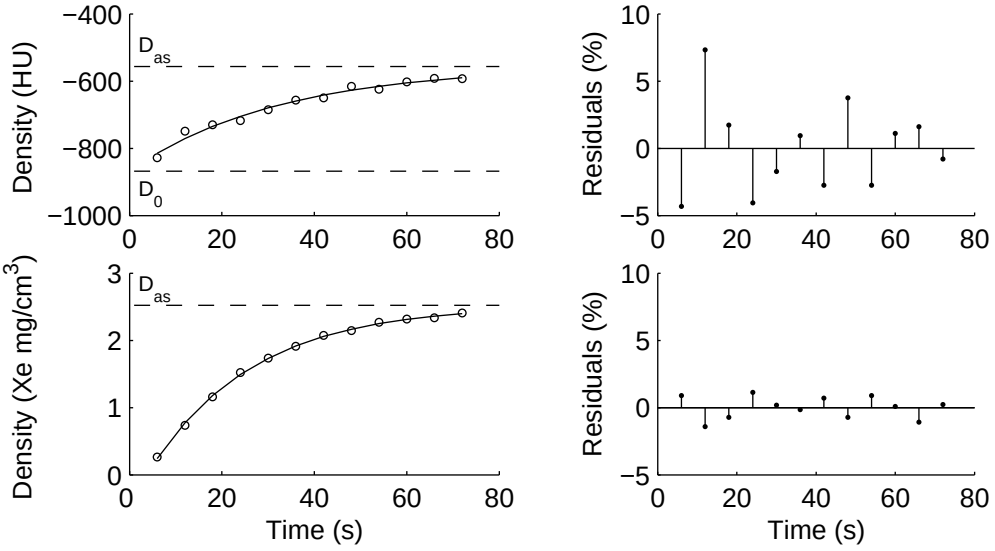

Fig. 5.9: Left images: The range of density change due to xenon, in a 5 x 5 pixel region. Upper a KES image, and lower a single energy transmission image in HU units. Right images: Residuals of the wash-in curves presented in the left.

6. DISCUSSION

The results obtained with the KES method were discussed in the preceding chapters and in the original publications **I- IV**. In the following these results are put in perspective by discussing the advantages and limitations of the KES method, and by making comparisons with other lung imaging methods. The discussion is concluded by an outlook and prospects of compact synchrotron radiation sources.

6.1 Advantages and limitations

K-edge subtraction imaging (KES) allows the observation of small anatomic structures carrying a tracer element, while removing practically all features due to other structures. A major advantage is that the results are quantitative. Unlike CT with standard x-ray sources, results are independent of changes in the lung tissue density, because the signal intensity on subtracted images depends only on xenon density. Spatial resolution is high (pixel size 0.35 mm and slice thickness 0.7 mm) and temporal resolution is fast enough to allow functional imaging (1s/image). In this method the signal contrast is high compared to the noise level. Radiation doses during imaging can be reduced to be compatible with the doses in clinical x-ray imaging. Because the method is quantitative, it is possible to estimate the distribution of ventilation even from a single KES image, but multiple breath imaging gives more exact results [Bayat et al., 2006].

However, there are some limitations with KES imaging method. The beam width is limited, which limits the maximum size of the object. At the medical beamline of the European Synchrotron Radiation Facility, the maximum beam width is 15.0 cm. Because the beam is stationary, the object needs to be rotated or moved trough the beams. Since KES requires narrow energy bands bracketing the K-absorption edge of the contrast element, sufficient flux is available only with the high-intensity synchrotron radiation sources. This gives limitations for the future clinical applications, before compact synchrotron sources are available at hospitals.

6.2 Comparison with other imaging methods

Scintigraphic methods use radioactive gases, and signal is recorded with gamma cameras, and with PET scanners. These methods are presented in section 2.3.3. Scintigraphic methods have been applied to study the changes in ventilation and perfusion in normal lungs [Vidal Melo et al., 2003] and after broncho-constriction [Vidal Melo et al., 2005] and [Venegas et al., 2005a]. The advantage of these methods is that scanners are available at hospital, but on the other hand the resolution is low compared to the KES imaging, and the contrast gases are radioactive.

Magnetic resonance imaging use hyperpolarized gases to study ventilation, and the method is presented in section 2.3.4. The advent of hyperpolarized gas MRI gives possibility to visualize ventilated airspaces of the lungs using wash-in of the contrast medium [Deninger et al., 2002] and [Kauczor et al., 2002]. However, ventilation is measured as fractional ventilation, which is a relative parameter [Spector et al., 2004]. Most MRI studies have been concentrated on visualizing the ventilation in healthy and diseased humans [Moller et al., 2002] and [Schreiber et al., 2005]. Spatial resolution of typical MRI scanners is low compared to the KES imaging, although it is possible to reach similar resolution with high-resolution small-animal MRI scanners.

Xenon-enhanced CT is a method, where distributions of ventilation are studied with multiple breath of xenon with a conventional CT scanner. The method is presented in section 2.3.5. The advantages of this method is that CT scanners are available at laboratories and hospitals. Xenon-enhanced CT has been used widely to study the distributions of ventilation with multiple breath models [Tajik et al., 2002], and ventilation and perfusion [Kreck et al., 2001] in healthy animals. The resolution with high-resolution CT scanners is of the same order as resolution in KES imaging. However, the signal intensity is low compared to the KES imaging, the results are not quantitative.

Fluorescent microspheres imaging method is applied for ventilation and perfusion studies. The method is presented in section 2.3.6. The method is very sensitive to study the distributions of ventilation [Robertson et al., 2005], and pulmonary blood flow [Robertson et al., 1997] and [Glenny et al., 2000], and their fractal properties. However, the collection of data is complicated and the experiments can not be repeated afterwards with the same animal, since the animal is sacrificed after the experiment. Moreover, it is difficult to study dynamical phenomena, like broncho-constriction with this method.

6.3 Compact synchrotron sources

Synchrotron radiation sources have revolutionized X-ray science with high-quality, intense X-ray beams. However, synchrotrons are large installations with circumferences of hundreds of meters, shared with many users for limited experiment times. Synchrotrons produce intense beams of nearly parallel, monochromatic radiation over a wide range of wavelengths. Laboratory x-ray sources produce much less intense, lower quality beams, but on the other hand, they are available at all research centers and hospitals. There is a growing need of compact x-ray sources to fill the gap between conventional laboratory x-ray sources and the synchrotron radiation sources.

Designs of compact synchrotron radiation sources have been based on two different concepts: reducing the size of storage rings with high-field superconducting bending magnets, or producing undulator radiation by interacting electron and laser beams. A 1.5 GeV storage ring could be reduced to a 5 m x 10 m rectangle with round corners of 4 T bending magnets, and sufficient flux of 35 keV radiation could be produced by a multipole 6 T superconducting wiggler [Oku et al., 1998]. A less expensive and potentially more intense source is obtained by placing a laser cavity in a low-energy storage ring. The laser pulse and the electron bunch collide at the center of the cavity at intervals of 13.3 ns, if the circumference of the ring is 4 m. Production of radiation can be described by considering the electron bunch to travel trough the "undulator" field of the laser pulse, or by Compton back-scattering of the laser photons from the electrons. The spectral brightness is expected to be comparable to that of 2nd generation synchrotron sources [Huang and Ruth, 1997]. A prototype is being commissioned [Giles, 2004].

Compact synchrotron sources will provide high-quality X-ray beams to the researchers in all fields of X-ray science. The brightness of the beam will be orders of magnitude below the beam available at 3rd generation synchrotron facilities, but is high enough to be used in many of the studies currently carried out at synchrotron facilities. This opens new possibilities especially in medical research, because new imaging techniques will be available at hospitals for clinical applications.

7. CONCLUSIONS

In this thesis a synchrotron radiation imaging method has been developed and used to study the structure and function of lungs in normal conditions and after histamine provocation in healthy anaesthetized rabbits. The studies demonstrate the feasibility of K-edge subtraction imaging (KES) for direct determination of regional ventilation, regional lung volumes, and airway structures. This is the first time that KES imaging with stable xenon gas has been used to study the lung structure and function using 2- and 3-dimensional CT.

The method was developed for imaging the ventilation of small animals. The spatial resolution is high, and the signal-to-noise ratio is much improved in KES images, when compared with single-energy images without subtraction. Therefore it is possible to detect small changes in the ventilated lung regions, and the calculation of regional wash-in time constants is accurate.

KES imaging technique was used to show that increasing tidal volume increases the uniformity of regional ventilation. The fractal properties of ventilation were calculated, and it was found that the fractal dimension varies in the lungs, and an estimate for the size of unit of ventilation was calculated.

The regional lung volumes were calculated from 3D spiral CT images, before and after histamine provocation. It was found that the ventilation is uniform at the baseline, but after histamine inhalation, the distribution became non-uniform, revealing poorly ventilated areas. Regional respiratory system compliance was calculated at baseline, and it was found to increase with the distance from the lung apex.

The kinetics of histamine-induced broncho-constriction were studied in proximal and distal airways. The results show patchy filling defects in peripheral lung ventilation following histamine provocation and that the distal airways react immediately to histamine and start to recover, while the reaction and the recovery in proximal airways is slower.

The application of synchrotron radiation technology to functional lung imaging offers unique possibilities for the non-invasive investigation of regional lung mechanics and physiology. This includes direct quantification of tracer elements, and dynamic respiration-gated image acquisition with excellent spatial resolu-

tion, allowing the exploration of regional lung function in small animal models such as rabbits, and rodents. This technique has the potential to address several unresolved issues of respiratory physiology including the relative contribution of acinar heterogeneity to overall ventilation heterogeneity, the size of the functional unit of ventilation, and the application of KES imaging to the simultaneous measurement of lung ventilation and perfusion, using inhaled xenon and injected iodine as contrast agents. Moreover, studies with sensitized animals will provide valuable information about the mechanisms of broncho-constriction.

The KES is available at many synchrotron radiation facilities, where it is used for research purposes. However, development of new compact synchrotron radiation sources will open new possibilities for clinical applications of synchrotron radiation imaging, including ventilation studies.

SUMMARY OF THE ARTICLES

The articles in this thesis are examples of how synchrotron radiation is used to functional medical imaging. The main aspects are the studies of the structure and function of lungs in normal or after airway narrowing by broncho-constriction. The role of respondent in wringing of the articles is explained in the following.

Article I [Bayat et al., 2001] introduces lung imaging with K-edge subtraction method (KES). This was the first publication of the group presenting the methods and basic images obtained with KES using inhaled stable xenon as contrast agent. The respondent took part in planning the experiment setup, the planning of the imaging protocol, and performing the experiments, and the respondent was responsible of developing the data analysis software and performing the data analysis. Reprinted with permission of Physics in Medicine and Biology. `http://www.iop.org/EJ/abstract/0031-9155/46/12/315/`.

Article II [Porra et al., 2004] shows the effect of tidal volume on ventilation distributions, based on wash-in imaging series. The respondent was responsible of planning the experiment setup, and the imaging protocol, performing the experiments, developing the data analysis software, performing the data analysis, and writing the article. Reprinted with permission of Journal of Applied Physiology. `http://jap.physiology.org/cgi/content/abstract/96/5/1899/`.

Article III [Monfraix et al., 2005] presents 3D imaging of the regional gas lung volume in normal and histamine provocated lungs with spiral CT. The respondent took part in the planning the experiment setup, planning the imaging protocol, performing the experiments, and the respondent performed a part of data analysis and writing. Reprinted with permission of Physics in Medicine and Biology. `http://www.iop.org/EJ/abstract/0031-9155/50/1/001/`.

Article IV [Bayat et al., 2006] presents how broncho-constriction produces caliber changes in bronchi and the associated changes in ventilation, and follows the changes with time. The respondent was responsible of planning the experiment setup, planning the imaging protocol, and performing the experiments, as well as of developing data analysis software, performing the data analysis, and most of the writing. Reprinted with permission of Journal of Applied Physiology. `http://jap.physiology.org/cgi/content/abstract/00594.2005v1/`.

BIBLIOGRAPHY

[Adam et al., 2003] Adam, J.-F., Elleaume, H., Le Duc, G., Corde, S., Charvet, A.-M., Tropres, I., Le Bas, J.-F., and Esteve, F. (2003). Absolute cerebral blood volume and blood flow measurements based on synchrotron radiation quantitative computed tomography. *J Cereb Blood Flow Metab*, 23(4):499–512.

[Als-Nielsen and McMorrow, 2001] Als-Nielsen, J. and McMorrow, D. (2001). *Elements of Modern X-ray Physics*. John Wiley & Sons, Ltd.

[Altemeier et al., 2000] Altemeier, W. A., McKinney, S., and Glenny, R. W. (2000). Fractal nature of regional ventilation distribution. *J Appl Physiol*, 88(5):1551–1557.

[Amirav et al., 1993] Amirav, I., Kramer, S. S., Grunstein, M. M., and Hoffman, E. A. (1993). Assessment of methacholine-induced airway constriction by ultrafast high-resolution computed tomography. *J Appl Physiol*, 75:2239–2250.

[Ball et al., 1962] Ball, W. B., Stewart Jr, P. B., Newsham, L. G. S., and Bates, D. V. (1962). Regional pulmonary function studied with xenon 133. *J Chlin Invest*, 41:519–531.

[Bassingthwaighte, 1988] Bassingthwaighte, J. B. (1988). Physiological heterogeneity: fractals link determinism and randomness in structures and functions. *News Physiol Sci*, 3:5–10.

[Bayat et al., 2001] Bayat, S., Le Duc, G., Porra, L., Berruyer, G., Nemoz, C., Monfraix, S., Fiedler, S., Thomlinson, W., Suortti, P., Standertskjöld-Nordenstam, C.-G., and Sovijärvi, A. R. A. (2001). Quantitative functional lung imaging with synchrotron radiation using inhaled xenon as contrast agent. *Phys Med Biol*, 46(12):3287–3299.

[Bayat et al., 2006] Bayat, S., Porra, L., Suhonen, H., Nemoz, C., Suortti, P., and Sovijärvi, A. R. A. (2006). Differences in the time course of proximal and distal airway response to inhaled histamine studied by synchrotron radiation CT. *J Appl Physiol*. in press February 9, 2006, doi:10.1152/japplphysiol.00594-2005.

[Bentley, 1995] Bentley, J. P. (1995). *Principles of measurement systems*. Longman, 3. edition.

[Benveniste and Blackband, 2002] Benveniste, H. and Blackband, S. (2002). MR microscopy and high resolution small animal MRI: applications in neuroscience research. *Prog Neurobiol*, 67(5):393–420.

[Bravin et al., 2003] Bravin, A., Fiedler, S., Coan, P., Labiche, J.-C., Ponchut, C., Peterzol, A., and Thomlinson, W. (2003). Comparison between a position sensitive germanium detector and a taper optics CCD "FRELON" camera for diffraction enhanced imaging. *Nucl Instr and Meth A*, 510:35–40.

[Brown et al., 1998] Brown, R. H., Georgakopoulos, J., and Mitzner, W. (1998). Individual canine airways responsiveness to aerosol histamine and methacholine in vivo. *Am J Respir Crit Care Med*, 157(2):491–497.

[Brown and Mitzner, 1998] Brown, R. H. and Mitzner, W. (1998). The myth of maximal airway responsiveness in vivo. *J Appl Physiol*, 85(6):2012–2017.

[Brown and Mitzner, 2003] Brown, R. H. and Mitzner, W. (2003). Functional imaging of airway narrowing. *Respir Physiol Neurobiol*, 137(2-3):327–337.

[Butler and Tsuda, 2005] Butler, J. P. and Tsuda, A. (2005). Logistic trajectory maps and aerosol mixing due to asynchronous flow at airway bifurcations. *Respir Physiol Neurobiol*, 148:195–206.

[Cho et al., 1993] Cho, C. H., Jones, J., and Singh, M. (1993). *Foundations of Medical Imaging*. John Wiley & Sons, New York.

[Chon et al., 2005] Chon, D., Simon, B. A., Beck, K. C., Shikata, H., Saba, O., Won, C., and Hoffman, E. A. (2005). Differences in regional wash-in and washout time constants for xenon-CT ventilation studies. *Respir Physiol Neurobiol*, 148(1-2):65–83.

[Cullity, 1978] Cullity, B. D. (1978). *Elements of X-ray diffraction*. Addison-Wesley, 2. edition.

[Dandurand et al., 1993] Dandurand, R. J., Wang, C. G., Phillips, N. C., and Eidelman, D. H. (1993). Responsiveness of individual airways to methacholine in adult rat lung explants. *J Appl Physiol*, 75:364–372.

[Darquenne and Paiva, 1994] Darquenne, C. and Paiva, M. (1994). One-dimensional simulation of aerosol transport and deposition in the human lung. *J Appl Physiol*, 77(6):2889–2898.

[Deninger et al., 2002] Deninger, A. J., Mansson, S., Petersson, J. S., Pettersson, G., Magnusson, P., Svensson, J., Fridlund, B., Hansson, G., Erjefeldt, I., Wollmer, P., and Golman, K. (2002). Quantitative measurement of regional lung ventilation using 3He MRI. *Magn Reson Med*, 48(2):223–232.

[Dingley et al., 1999] Dingley, J., Ivanova-Stoilova, T., and Grundler, S. (1999). Xenon: recent developments. *Anaesthesia*, 54:335–346.

[Ebashi et al., 1991] Ebashi, S., Koch, M., and Rubinstein, E., editors (1991). *Handbook of Synchrotron Radiation*, volume 4. Elsevier Science Publishers B. V.

[Elleaume et al., 1999] Elleaume, H., Charvet, A.-M., Berkvens, P., Berruyer, G., Brochard, T., Dabin, Y., Dominguez, M. C., Draperi, A., Fiedler, S., Goujon, G., Duc, G. L., Mattenet, M., Nemoz, C., Perez, M., Renier, M., Schulze, C., Spanne, P., Suortti, P., Thomlinson, W., Esteve, F., Bertrand, B., and Bas, J.-F. L. (1999). Instrumentation of the esrf medical imaging facility. *Nucl Instr and Meth A*, 428:513–527.

[Elleaume et al., 2002] Elleaume, H., Charvet, A.-M., Corde, S., Esteve, F., and Le Bas, J.-F. (2002). Performance of computed tomography for contrast agent concentration measurements with monochromatic x-ray beams: comparison of K-edge versus temporal subtraction. *Phys Med Biol*, 47(18):3369–3385.

[Elleaume et al., 1997] Elleaume, H., Charvet, A.-M., and Le Bas, J.-F. (1997). The synchrotron beam, a new dimension for contrast media research? *Acta Radiol Suppl*, 412:29–41.

[Elleaume et al., 2000] Elleaume, H., Fiedler, S., Esteve, F., Bertrand, B., Charvet, A.-M., Berkvens, P., Berruyer, G., Brochard, T., Le Duc, G., Nemoz, C., Renier, M., Suortti, P., Thomlinson, W., and Le Bas, J.-F. (2000). First human transvenous coronary angiography at the European Synchrotron Radiation Facility. *Phys Med Biol*, 45(9):39–43.

[Engel, 1986] Engel, L. A. (1986). *Handbook of Physiology*. Bethesda.

[Frerichs et al., 2002] Frerichs, I., Hinz, J., Herrmann, P., Weisser, G., Hahn, G., Dudykevych, T., Quintel, M., and Hellige, G. (2002). Detection of local lung air content by electrical impedance tomography compared with electron beam CT. *J Appl Physiol*, 93(2):660–666.

[Gefter, 2002] Gefter, W. (2002). Functional ct imaging of the lungs: the pulmonary function test of the new millennium. *Acad Radiol*, 9:127–129.

[Giacomini et al., 1998] Giacomini, J. C., Gordon, H., O'Neil, R., Kessel, A. V., Cason, B., Chapman, D., Lavendar, W., Gmur, N., Menk, R., Thomlinson, W., Zhong, Z., and Rubenstein, E. (1998). Bronchial imaging in humans using xenon k-edge dichromography. *Nucl Instr and Meth A*, 406:473–478.

[Giles, 2004] Giles, J. (2004). Lasers bend beams for desktop x-ray source. *Nature*, 428:789.

[Gillis and Lutchen, 1999] Gillis, H. L. and Lutchen, K. R. (1999). How heterogeneous bronchoconstriction affects ventilation distribution in human lungs: a morphometric model. *Ann Biomed Eng*, 27:1–13.

[Glenny et al., 2000] Glenny, R. W., Bernard, S. L., and Robertson, H. T. (2000). Pulmonary blood flow remains fractal down to the level of gas exchange. *J Appl Physiol*, 89:742–748.

[Glenny and Robertson, 1990] Glenny, R. W. and Robertson, H. T. (1990). Fractal properties of pulmonary blood flow: characterization of spatial heterogeneity. *J Appl Physiol*, 69(2):532–545.

[Glenny et al., 1991] Glenny, R. W., Robertson, H. T., Yamashiro, S., and Bassingthwaighte, J. B. (1991). Applications of fractal analysis to physiology. *J Appl Physiol*, 70(6):2351–2367.

[Goldberger and West, 1987] Goldberger, A. L. and West, B. J. (1987). Fractals in physiology and medicine. *Yale J Biol Med*, 60:421–435.

[Gray, 1918] Gray, H. (1918). *Anatomy of the human body, by Henry Gray.* Philadelphia: Lea & Febiger.

[Guerrero et al., 2006] Guerrero, T., Sanders, K., Castillo, E., Zhang, Y., Bidaut, L., Pan, T., and Komaki, R. (2006). Dynamic ventilation imaging from four-dimensional computed tomography. *Phys Med Biol*, 51:777–791.

[Gur et al., 1979] Gur, D., Drayer, B. P., Borovetz, H. S., Griffith, B. P., Hardesty, R. L., and Wolfson, S. K. (1979). Dynamic computed tomography of the lung: regional ventilation measurements. *J Comput Assist Tomogr*, 3:749–753.

[Gur et al., 1981] Gur, D., Shabason, L., Borovetz, H. S., Herbert, D. L., Reece, G. J., Kennedy, W. H., and Serago, C. (1981). Regional pulmonary ventilation measurements by xenon-enhanced dynamic computed tomography: an update. *J Comput Assist Tomogr*, 5:678–683.

[Haefeli-Bleuer and Weibel, 1988] Haefeli-Bleuer, B. and Weibel, E. R. (1988). Morphometry of the human pulmonary acinus. *Anat Rec*, 220:401–414.

[Hatabu et al., 2001] Hatabu, H., Tadamura, E., Chen, Q., Stock, K. W., Li, W., Prasad, P. V., and Edelman, R. R. (2001). Pulmonary ventilation: dynamic MRI with inhalation of molecular oxygen. *Eur J Radiol*, 37(3):172–178.

[Horsfield, 1990] Horsfield, K. (1990). Diameters, generations, and orders of branches in the bronchial tree. *J Appl Physiol*, pages 457–461.

[Horsfield et al., 1971] Horsfield, K., Dart, G., Olson, D. E., Filley, G. F., and Cumming, G. (1971). Models of the human bronchial tree. *J Appl Physiol*, 31:202–217.

[Huang and Ruth, 1997] Huang, Z. and Ruth, R. D. (1997). Laser-electron storage ring as a compact source of high-intensity x-rays. 19th International Free Electron Laser Conference, Beijing, China, SLAC-PUB-7677.

[Jacobson, 1953] Jacobson, B. (1953). Dichromatic absorption radiography; dichromography. *Acta Radiol*, 39(6):437–452.

[Johnson and Hedlund, 1996] Johnson, G. A. and Hedlund, L. W. (1996). Functional imaging of the lung. *Nat Med*, 2(11):1192. Comment.

[Kak and Slaney, 1988] Kak, A. C. and Slaney, M. (1988). *Principales of Computerized Tomographic Imaging*. IEEE press. http://www.slaney.org/pct/index.html.

[Kauczor, 2003] Kauczor, H.-U. (2003). Hyperpolarized helium-3 gas magnetic resonance imaging of the lung. *Top Magn Reson Imaging*, 14(3):223–230.

[Kauczor et al., 2002] Kauczor, H.-U., Hanke, A., and Van Beek, E. J. R. (2002). Assessment of lung ventilation by MR imaging: current status and future perspectives. *Eur Radiol*, 12(8):1962–1970.

[Kitaoka and Suki, 1997] Kitaoka, H. and Suki, B. (1997). Branching design of the bronchial tree based on a diameter-flow relationship. *J Appl Physiol*, 82(3):968–976.

[Kitaoka et al., 1999] Kitaoka, H., Takaki, R., and Suki, B. (1999). A three-dimension model of the human airway tree. *J Appl Physiol*, 87:2207–2217.

[Kitaoka et al., 2000] Kitaoka, H., Tamura, S., and Takaki, R. (2000). A three-dimensional model of the human pulmonary acinus. *J Appl Physiol*, 88:2260–2268.

[Kreck et al., 2001] Kreck, T. C., Krueger, M. A., Altemeier, W. A., Sinclair, S. E., Robertson, H. T., Shade, E. D., Hildebrandt, J., Lamm, W. J., Frazer, D. A., Polissar, N. L., and Hlastala, M. P. (2001). Determination of regional ventilation and perfusion in the lung using xenon and computed tomography. *J Appl Physiol*, 91(4):1741–1749.

[Le Duc et al., 2000] Le Duc, G., Corde, S., Elleaume, H., Esteve, F., Charvet, A.-M., Brochard, T., Fiedler, S., Collomb, A., and Le Bas, J.-F. (2000). Feasibility of synchrotron radiation computed tomography on rats bearing glioma after iodine or gadolinium injection. Jeune Equipe RSRM-UJF. *Eur Radiol*, 10(9):1487–1492.

[Lewis, 2004] Lewis, R. A. (2004). Medical phase contrast x-ray imaging: current status and future prospects. *Phys Med Biol*, 49(16):3573–3583.

[Limpert et al., 2001] Limpert, E., Werner, A. S., and Abbt, M. (2001). Log-normal distributions across the sciences: keys and clues. *Bioscience*, 51:341–352.

[Lumb, 2000] Lumb, A. B. (2000). *Nunn's Applied Respiratory Physiology*. Butterworth Heinemann, 5. edition.

[Majumdar et al., 2005] Majumdar, A., Alencar, A. M., Buldyrev, S. V., Hantos, Z., Lutchen, K. R., Stanley, H. E., and Suki, B. (2005). Relating airway diameter distributions to regular branching asymmetry in the lung. *Phys Rev Lett*, 95(16):168101 1–4.

[Mandelbrot, 1983] Mandelbrot, B. (1983). *The fractal geometry of nature*. W.H. Freeman and Company, updated edition.

[Marcucci et al., 2001] Marcucci, C., Nyhan, D., and Simon, B. A. (2001). Distribution of pulmonary ventilation using Xe-enhanced computed tomography in prone and supine dogs. *J Appl Physiol*, 90(2):421–430. Evaluation Studies.

[Martin et al., 1996] Martin, C., Uhlig, S., and Ullrich, V. (1996). Videomicroscopy of methacholine-induced contraction of individual airways in precision-cut lung slices. *Eur Respir J*, 9:2479–2487.

[Marttila, 1995] Marttila, O. J. (1995). *Säteilysuojelun perusteet*. Limes ry:n graafiset laitokset, 2. edition.

[Mauroy et al., 2004] Mauroy, B., Filoche, M., Weibel, E. R., and Sapoval, B. (2004). An optimal bronchial tree may be dangerous. *Nature*, 427:633–636.

[Melsom et al., 1997] Melsom, M. N., Kramer-Johansen, J., Flatebo, T., Muller, C., and Nicolaysen, G. (1997). Distribution of pulmonary ventilation and perfusion measured simultaneously in awake goats. *Acta Physiol Scand*, 159:199–208.

[Middleton et al., 1995] Middleton, H., Black, R., Saam, B., Gates, G., Cofer, G., Guenther, B., Happer, W., Hedlund, L., Johnson, G adn Juvan, K., and Swartz, J. (1995). Mr imaging with hyperpolarized he-3 gas. *Magn Reson Med*, 33:271–275.

[Milic-Emili et al., 1966] Milic-Emili, J., Henderson, J. A. M., Dolowich, M. B., Trop, D., and Kaneko, K. (1966). Regional distribution of inspired gas in the lung. *J Appl Physiol*, 21:749–759.

[Moller et al., 2002] Moller, H. E., Chen, X. J., Saam, B., Hagspiel, K. D., Johnson, G. A., Altes, T. A., de Lange, E. E., and Kauczor, H.-U. (2002). MRI of the lungs using hyperpolarized noble gases. *Magn Reson Med*, 47(6):1029–1051.

[Monfraix, 2004] Monfraix, S. (2004). *Mise au point d'une nouvelle technique d'imagerie fonctionnelle pulmonaire en tomographie quantitative par rayonnement synchrotron*. PhD thesis, Universite Joseph Fourier Grenoble.

[Monfraix et al., 2005] Monfraix, S., Bayat, S., Porra, L., Berruyer, G., Nemoz, C., Thomlinson, W., Suortti, P., and Sovijärvi, A. R. A. (2005). Quantitative measurement of regional lung gas volume by synchrotron radiation computed tomography. *Phys Med Biol*, 50(1):1–11.

[Nienstedt et al., 1992] Nienstedt, W., Hänninen, O., Arstila, A., and Björkqvist, S.-E. (1992). *Ihmisen Fysiologia ja Anatomia*. WSOY, 8. edition.

[NIST, 2005] NIST (2005). National institute of standards and technology. Physical reference data. http://physics.nist.gov/PhysRefData/.

[Oku et al., 1998] Oku, Y., Hyodo, K., Ando, M., Zhong, Z., and Thomlinson, W. (1998). *Medical Applications of Synchrotron Radiation*, chapter Contrast analysis in coronary images using 2D monochromatic x-rays optimized dedicated synchrotron IVCA system. Springer-Verkag Tokyo.

[Oros and Shah, 2004] Oros, A.-M. and Shah, N. J. (2004). Hyperpolarized xenon in NMR and MRI. *Phys Med Biol*, 49:R105–R153.

[Paiva and Engel, 1984] Paiva, M. and Engel, L. A. (1984). Model analysis of gas distribution within human lung acinus. *J Appl Physiol*, 56:418–425.

[Paiva and Engel, 1987] Paiva, M. and Engel, L. A. (1987). Theoretical studies of gas mixing and ventilation distribution in the lung. *Physiol Rev*, 67(3):750–796.

[Pan et al., 2005] Pan, T., Mawlawi, O., Nehmeh, S. A., Erdi, Y. E., Luo, D., Liu, H. H., Castillo, R., Mohan, R., Liao, Z., and Macapinlac, H. A. (2005). Attenuation correction of PET images with respiration-averaged CT images in PET/CT. *J Nucl Med*, 46(9):1481–1487. Clinical Trial.

[Petak et al., 1997] Petak, F., Hantos, Z., Adamicza, A., Asztalos, T., and Sly, P. D. (1997). Methacholine-induced bronchoconstriction in rats: effects of intravenous vs. aerosol delivery. *J Appl Physiol*, 82:1479–1487.

[Peterzol et al., 2003] Peterzol, A., Bravin, A., Coan, P., and Elleaume, H. (2003). Image quality evaluation of the angiography imaging system at the european synchrotron radiation facility. *Nuclear Instruments and Methods in Physics Research A*, 510:45–50.

[Porra et al., 2006] Porra, L., Bayat, S., Suhonen, H., Nemoz, C., Sovijärvi, A. R. A., and Suortti, P. (2006). Fractal structure and ventilation distributions of lungs studied by synchrotron radiation. *Manuscript*. Manuscript.

[Porra et al., 2004] Porra, L., Monfraix, S., Berruyer, G., Le Duc, G., Nemoz, C., Thomlinson, W., Suortti, P., Sovijärvi, A. R. A., and Bayat, S. (2004). Effect of tidal volume on distribution of ventilation assessed by synchrotron radiation CT in rabbit. *J Appl Physiol*, 96(5):1899–1908.

[Robertson et al., 1997] Robertson, H. T., Glenny, R. W., Stanford, D., McInnes, L. M., Luchtel, D. L., and Covert, D. (1997). High-resolution maps of regional ventilation utilizing inhaled fluorescent microspheres. *J Appl Physiol*, 82(3):943–953.

[Robertson et al., 2005] Robertson, H. T., Kreck, T., and Krueger, M. (2005). The spatial and temporal heterogeneity of regional ventilation: Comparison of measurements by two high-resolution methods. *Respir physiol Neurobiol*, 148:85–95.

[Rodriguez et al., 1987] Rodriguez, M., Bur, S., Favre, A., and Weibel, E. R. (1987). Pulmonary acinus: geometry and morphometry of the peripheral airway system in rat and rabbit. *Am J Anat*, 180(2):143–155.

[Rubenstein et al., 1990] Rubenstein, E., Giacomini, J. C., Gordon, H., Thompson, A., Brown, G., Hofstadter, R., Thomlinson, W., and Zeman, H. (1990). Synchrotron radiation coronary angiography with a dual-beam dual-detector imaging system. *Nucl Instr and Meth A*, 291:80–85.

[Rubenstein et al., 1986] Rubenstein, E., Hofstadter, R., Zeman, H. D., Thompson, A. C., Otis, J. N., Brown, G. S., Giacomini, J. C., Gordon, H. J., Kernoff, R. S., Harrison, D. C., and Thomlinson, W. (1986). Transvenous coronary angiography in humans using synchrotron radiation. *Proc Natl Acad Sci USA*, 83(24):9724–9728.

[Ruiz-Cabello et al., 2005] Ruiz-Cabello, J., Perez-Sanchez, J. M., Perez de Alejo, R., Rodriguez, I., Gonzalez-Mangado, N., Peces-Barba, G., and Cortijo, M. (2005). Diffusion-weighted 19F-MRI of lung periphery: Influence of pressure and air-SF6 composition on apparent diffusion coefficients. *Respir Physiol Neurobiol*, 148(1-2):43–56.

[Sapoval et al., 2002] Sapoval, B., Filoche, M., and Weibel, E. R. (2002). Smaller is better–but not too small: a physical scale for the design of the mammalian pulmonary acinus. *Proc Natl Acad Sci U S A*, 99(16):10411–10416.

[Schreiber et al., 2005] Schreiber, W. G., Morbach, A. E., Stavngaard, T., Gast, K. K., Herweling, A., Sogaard, L. V., Windirsch, M., Schmiedeskamp, J., Heussel, C. P., and Kauczor, H.-U. (2005). Assessment of lung microstructure with magnetic resonance imaging of hyperpolarized Helium-3. *Respir Physiol Neurobiol*, 148(1-2):23–42. Evaluation Studies.

[Simon et al., 1998] Simon, B. A., Marcucci, C., Fung, M., and Lele, S. R. (1998). Parameter estimation and confidence intervals for Xe-CT ventilation studies: a Monte Carlo approach. *J Appl Physiol*, 84(2):709–716.

[Sovijarvi et al., 1982] Sovijarvi, A. R., Poyhonen, L., Kellomaki, L., and Muittari, A. (1982). Effects of acute and long-term bronchodilator treatment on regional lung function in asthma assessed with krypton-81m and technetium-99m-labelled macroaggregates. *Thorax*, 37(7):516–520.

[Sovijärvi et al., 2003] Sovijärvi, A., Ahonen, A., Hartiala, J., Länsimies, E., Savolainen, S., Turjanmaa, V., and Vanninen, E., editors (2003). *Kliininen fysiologia ja isotooppilääketiede*. Duodecim, 1. edition.

[Spector et al., 2004] Spector, Z. Z., Emami, K., Fischer, M. C., Zhu, J., Ishii, M., Yu, J., Kadlecek, S., Driehuys, B., Panettieri, R. A., Lipson, D. A., Gefter, W., Shrager, J., and Rizi, R. R. (2004). A small animal model of regional alveolar ventilation using HP 3He MRI. *Acad Radiol*, 11(10):1171–1179.

[Suortti and Thomlinson, 2003] Suortti, P. and Thomlinson, W. (2003). Medical applications of synchrotron radiation - topical review. *Phys Med Biol*, 48:R1–R35.

[Suortti et al., 1993] Suortti, P., Thomlinson, W., Chapman, D., Gmür, N., Siddons, D. P., and Schulze, C. (1993). A single crystal bent Laue monochromator for coronary angiography. *Nucl Instr and Meth A*, 336:304–309.

[Tai and Laforest, 2005] Tai, Y.-C. and Laforest, R. (2005). Instrumentation aspects of animal PET. *Annu Rev Biomed Eng*, 7:255–285.

[Tajik et al., 2002] Tajik, J. K., Chon, D., Won, C., Tran, B. Q., and Hoffman, E. A. (2002). Subsecond multisection CT of regional pulmonary ventilation. *Acad Radiol*, 9(2):130–146.

[Takezawa et al., 1980] Takezawa, J., Miller, F. J., and O'Neil, J. J. (1980). Single-breath diffusing capacity and lung volumes in small laboratory mammals. *J Appl Physiol*, 48(6):1052–1059.

[Thomlinson et al., 2005] Thomlinson, W., Suortti, P., and Chapman, D. (2005). Recent advances in synchrotron radiation medical research. *Nuclear Instruments and Methods in Physics Research A*, 543:288–296.

[Thomlinson, 1996] Thomlinson, W. C. (1996). Transvenous coronary angiography in humans. Proc. International School of Physics. Enrico Fermi'-Course CXXVIII-Biomedical Applications of Synchrotron Radiation.

[Treppo et al., 1997] Treppo, S., Mijailovich, S. M., and Venegas, J. G. (1997). Contributions of pulmonary perfusion and ventilation to heterogeneity in $\dot{V}_a/\dot{Q}$ measured by pet. *J Appl Physiol*, 82:1163–1176.

[Venegas et al., 2005a] Venegas, J. G., Schroeder, T., Harris, S., Winkler, R. T., and Melo, M. F. V. (2005a). The distribution of ventilation during bronchoconstriction is patchy and bimodal: a PET imaging study. *Respir Physiol Neurobiol*, 148(1-2):57–64.

[Venegas et al., 2005b] Venegas, J. G., Winkler, T., Musch, G., Vidal Melo, M. F., Layfield, D., Tgavalekos, N., Fischman, A., Callahan, R. J., Bellani, G., and Harris, R. S. (2005b). Self-organized patchiness in asthma as a prelude to catastrophic shifts. *Nature*, 434(7034):777–782.

[Viallon et al., 1999] Viallon, M., Cofer, G. P., Suddarth, S. A., Moller, H. E., Chen, X. J., Chawla, M. S., Hedlund, L. W., Cremillieux, Y., and Johnson, G. A. (1999). Functional MR microscopy of the lung using hyperpolarized 3He. *Magn Reson Med*, 41(4):787–792.

[Vidal Melo et al., 2005] Vidal Melo, M. F., Harris, R. S., Layfield, J. D. H., and Venegas, J. G. (2005). Topographic basis of bimodal ventilation-perfusion

distributions during bronchoconstriction in sheep. *Am J Respir Crit Care Med*, 171(7):714–721.

[Vidal Melo et al., 2003] Vidal Melo, M. F., Layfield, D., Harris, R. S., O'Neill, K., Musch, G., Richter, T., Winkler, T., Fischman, A. J., and Venegas, J. G. (2003). Quantification of regional ventilation-perfusion ratios with PET. *J Nucl Med*, 44(12):1982–1991. Evaluation Studies.

[Weibel, 1963] Weibel, E. R. (1963). *Morphometry of the Human Lung*. SpringerVerlag Academic Press, Heidelberg, New York.

[Weibel et al., 2005] Weibel, E. R., Sapoval, B., and Filoche, M. (2005). Design of peripheral airways for efficient gas exchange. *Respir Physiol Neurobiol*, 148:3–21.

[West et al., 1997] West, G. B., Brown, J. H., and Enquist, B. J. (1997). A general model for the origin of allometric scaling laws in biology. *Science*, 276:122–126.

[Wohlsen et al., 2003] Wohlsen, A., Martin, C., Vollmer, E., Branscheid, D., Magnussen, H., Becker, W., Lepp, U., and Uhlig, S. (2003). The early allergic response in small airways of human precision-cut lung slices. *Eur Respir J*, 21:1024–1032.

[Wohlsen et al., 2001] Wohlsen, A., Uhlig, S., and Martin, C. (2001). Immediate allergic response in small airways. *Am J Respir Crit Care Med*, 163(6):1462–1469.

[Yonas et al., 1981] Yonas, H., Grundy, B., Gur, D., Shabason, L., Wolfson, S. J., and Cook, E. (1981). Side effects of xenon inhalation. *J Comput Assist Tomogr*, 5:591–592.

[Zeltner et al., 1991] Zeltner, T. B., Sweeney, T. D., Skornik, W. A., Feldman, H. A., and D, B. J. (1991). Retention and clearance of 0.9-μm particles inhaled by hamsters during rest or exercise. *J Appl Physiol*, 70:1137–1145.